# DISCLAIMER

This report was prepared as an account of work sponsored by an agency of the United States Government. Neither the United States Government nor any agency thereof, nor any of their employees, makes any warranty, express or implied, or assumes any legal liability or responsibility for the accuracy, completeness, or usefulness of any information, apparatus, product, or process disclosed, or represents that its use would not infringe privately owned rights. Reference herein to any specific commercial product, process, or service by trade name, trademark, manufacturer, or otherwise does not necessarily constitute or imply its endorsement, recommendation, or favoring by the United States Government or any agency thereof. The views and opinions of authors expressed herein do not necessarily state or reflect those of the United States Government or any agency thereof. Reference herein to any social initiative (including but not limited to Diversity, Equity, and Inclusion (DEI); Community Benefits Plans (CBP); Justice 40; etc.) is made by the Author independent of any current requirement by the United States Government and does not constitute or imply endorsement, recommendation, or support by the United States Government or any agency thereof.

INL/EXT-21-01568

# Depletion Benchmark of the AFIP-7 Experiment in the Advanced Test Reactor

February 2025

Joseph Nielsen, PhD, PE
Brittany Grayson, PhD
*Idaho National Laboratory*

**INL/EXT-21-01568**

# Depletion Benchmark of the AFIP-7 Experiment in the Advanced Test Reactor

**Joseph Nielsen, PhD, PE**
**Brittany Grayson**
**Idaho National Laboratory**

**February 2025**

**Idaho National Laboratory**
**Nuclear Science and Technology**
**Idaho Falls, Idaho 83415**

**http://www.inl.gov**

**Prepared for the**
**U.S. Department of Energy**
**Office of Nuclear Energy**
**Under DOE Idaho Operations Office**
**Contract DE-AC07-05ID14517**

*Page intentionally left blank*

# ABSTRACT

Reactor physics depletion benchmarks for low-enriched uranium fuel are limited in number. In particular, there is very limited data for LEU benchmarks for U-10Mo (Uranium-10% Molybdenum) plate fuel developed for use in U.S. high-performance research reactors (USHPRR). USHPRR includes the Advanced Test Reactor (ATR), Advanced Test Reactor Critical Facility (ATR-C), High Flux Isotope Reactor (HFIR), University of Missouri Research Reactor (MURR), Massachusetts Institute of Technology Reactor (MITR), and National Bureau of Standards Reactor (NBSR) at the National Institute of Science and Technology. These reactors are fueled with high-enriched uranium dispersed fuel in a silicon/aluminum matrix. In support of conversion to a HALEU fuel, qualification of U-10Mo formed into a monolithic foil is being performed. Fuel qualification involves irradiated fueled specimens in the ATR. The irradiation tests provide an opportunity to benchmark depletion capabilities of reactor physics codes in support of the ATR operation, as well as develop benchmarks that can be used by other institutions to benchmark other reactor physics codes. This report documents the development of a benchmark model of the irradiation of the ATR Full -size plate In center flux trap Position 7 (AFIP-7) experiment.

*Page intentionally left blank*

# CONTENTS

# FIGURES

# TABLES

*Page intentionally left blank*

# ACRONYMS

| | |
|---|---|
| AD | Atom densities |
| AFC | Advanced Fuel Cycle |
| AFIP | ATR Full size plate In center Flux trap Position |
| ATR | Advanced Test Reactor |
| BOC | Beginning of Cycle |
| CDIPT | Chopped dummy in-pile tube |
| CFT | Center Flux Trap |
| CMCDT | Common Monte Carlo design tool |
| HALEU | High-Assay Low-Enriched Uranium |
| HFIR | High Flux Isotope Reactor |
| HNF | Heating normalization factor |
| HPRR | High-Performance Research Reactor |
| HSA | High specific activity |
| HSIS | Hydraulic Shuttle Irradiation System |
| IPT | In-Pile Tube |
| LEU | Low-Enriched Uranium |
| LSA | Low Specific Activity |
| MITR | Massachusetts Institute of Technology Reactor |
| MURR | University of Missouri Research Reactor |
| NBSR | National Bureau of Standards Reactor |
| NFCF | Neutron flux conversion factor |
| OSCC | Outer Shim Control Cylinders |
| PIE | Post-Irradiation Examination |
| RERTR | Reduced Enrichment for Research and Test Reactors |
| SFT | South Flux Trap |
| SIHA | Standard irradiation housing assembly |
| SIPT | Standard In-Pile Tube |
| U-10Mo | Uranium 10wt% Molybdenum |

*Page intentionally left blank*

# 1. INTRODUCTION

This report's purpose is to document the low-enriched uranium (LEU) benchmark depletion analysis of the ATR Full-size plate In center flux trap Position 7 (AFIP-7) experiment. The AFIP-7 experiment was irradiated in the Advanced Test Reactor (ATR) during Cycles 149B and 150B. The experiment consisted of four curved fuel plates with an activate fuel length of 38.5 in. The nominal fuel zone of the four plates consisted of 19.75 wt.% enriched U-10Mo monolithic fuel core with a thickness of 0.013 in.

This report documents the as-irradiated conditions of the AFIP-7 experiment in the ATR and compares the calculated results to the measured post-irradiation examination (PIE) data. This report may be used in future analysis to validate various reactor physics codes in support of U-10Mo LEU fuel systems. This analysis uses the MC21 code developed by the Naval Nuclear Laboratory (NNL) [1]. MC21 is a three-dimensional Monte Carlo neutron transport code with full depletion capabilities. The code was selected as it is a continuous energy high-fidelity neutron transport code. This allows for future comparisons between low-fidelity/order codes.

The benchmark model used in this report contains a detailed model of the AFIP-7 experiment. Experiment models in other positions have been simplified. A higher fidelity model has been created—though, details of the model cannot be made available and are not shared in this report. A comparison of calculated eigenvalues and power splits between the benchmark model and the more detailed model is documented in this report.

The benchmark and higher fidelity models of the AFIP-7 experiment are depleted using the ATR operating conditions that are summarized in this report. The data for the AFIP-7 depletion analysis has been extracted and compared to PIE data. Power density data calculated from MC21 is reported in this report. Calculated fission density and U-235 depletion are compared to PIE data.

# 2. ATR MODEL

In this report, a 1994 Core Internals Changeout (94CIC) model [2] is used as a starting point. The 94CIC model consists of a core of 40 fresh fuel elements, water filled flux traps and fillers in various experiment positions. The intent of the configuration is to perform low power physics measurements following replacement of the primary core components (e.g., reflector, control components, etc.) Using the 94CIC model, experiment positions were replaced with representative configurations to better represent the ATR core for the operating Cycles 149B and 150B to create a benchmark model. Experiments models have been incorporated into a higher fidelity model—though, they cannot be made available in this report. The cycle models that contain these experiments are referred to in this report as the explicit model. Model results relevant to the AFIP-7 benchmark results are presented in this report, which would include eigenvalue, lobe powers, and AFIP-7 power and burnup. The results of the explicit model are compared to the benchmark model, which allows for individuals to compare computational bias between actual data, the explicit or best representative model, and the benchmark model.

The PUMA software package was used to develop the benchmark and explicit models for MC21. PUMA is part of the common Monte Carlo design tool, which includes MC21. PUMA is a JAVA-based application programming interface (API) that allows users to develop models based on combinatorial geometry. Execution of PUMA creates the MC21 input files. A listing of experiments used in the model in this report is contained in Table 1.

The benchmark and explicit models contain a detailed fuel loading developed from the ATR fuel element database that is used to support core physics analysis at ATR. The database was developed to provide detailed composition data for recycled fuel elements. A summary of the gram loading for each fuel element of each operating cycle is provided in this report.

The ATR is high-flux beryllium-reflected reactor. The Be-9 isotope transmutes to He-3 and H-3 through a series of $(n,\alpha)$ reactions, including Li-6, which has a relatively high cross-section (~941 b) [3]. The He-3 has a large (n,p) cross section, which produces H-3, which in turn decays to He-3. Both Li-6 an He-4  provide significant amounts of negative reactivity in the ATR over prolonged operation. The benchmark and explicit models account for the amount of activation and buildup of H-3, Li-6 and He-3 in the reactor. The isotopic composition for the beryllium is provided in Appendix C.

In addition to the buildup of Li-6, H-3, and He-3 in the reflector, the hafnium control components (i.e., neckshims and outer shim control cylinders) experience depletion during irradiation. As such, the hafnium compositions have been depleted and beginning of cycle compositions are provided in Appendix C.

Detailed models of the major ATR components are provided in [2]. The major components include fuel elements, reflector, control components, and in-pile tubes. Some of the experiment hardware is described in [2]; however, changes will be described in this report. A summary of experiment loading between [2] and the benchmark model for Cycle 149B is provided in Table 1. It should be noted that proprietary experiments are not modeled in the benchmark model as information cannot be published. A summary of experiment loading between [4] and the benchmark model for Cycle 150B is provided in Table 2. Appendix A describes the experiment models that are not included in [2]. A reference to the description of the experiment model details is provided in Table 1.

Table 1. Experiment loading for Cycle 149B used in the benchmark models [2] [5] [6].

| Position | 94CIC Experiment | Experiment Loading | Comments | Reference/Section Description |
|---|---|---|---|---|
| SWFT | EmptySIPT | SE100_SW100 | Empty SIPT filled with standard backup | A.2 |
| SEFT | EmptySIPT | SE100_SW100 | Empty SIPT filled with standard backup | A.2 |
| NFT | EmptySIPT | N100 | Empty SIPT filled with standard backup | A.2 |
| WFT | EmptySIPT | N100 | Empty SIPT filled with standard backup | A.2 |
| NEFT | LIHA103 | LIHA103 | Large irradiation housing assembly used during CIC | Reference [2] Figure 35 |
| CFT | CIHA103 | AFIP7 | AFIP-7 Experiment | 3 |
| EFT | SIHA103 | SIHA145 | 149B/150B irradiation contains advanced fuel cycle baskets. | A.5, Reference [2] Figure 37 |
| SFT | SIHA103 | AGC2 | Advanced Graphite-2 experiment. | A.4 |
| NWFT | NWFiller | NW100 | NW-100 is the standard large in-pile tube backup assembly | A.3 |
| A1 | SFR | HHSACO | High specific activity in place of solid flow restrictor | A.6 |
| A2 | SFR | HHSACO | High specific activity in place of solid flow restrictor | A.6 |
| A3 | SFR | SFR | Solid flow restrictor | Reference [2] Figure 38 |
| A4 | SFR | HHSACO | High specific activity in place of solid flow restrictor | A.6 |
| A5 | SFR | HHSACO | High specific activity in place of solid flow restrictor | A.6 |
| A6 | SFR | HHSACO | High specific activity in place of solid flow restrictor | A.6 |
| A7 | SFR | HHSACO | High specific activity in place of solid flow restrictor | A.6 |
| A8 | SFR | HHSACO | High specific activity in place of solid flow restrictor | A.6 |

Table 1. Experiment loading for Cycle 149B used in the benchmark models [2] [5] [6].

| Position | 94CIC Experiment | Experiment Loading | Comments | Reference/Section Description |
|---|---|---|---|---|
| A9 | SFR | HHSACO | High specific activity in place of solid flow restrictor | A.6 |
| A10 | SFR | HHSACO | High specific activity in place of solid flow restrictor | A.6 |
| A11 | SFR | HHSACO | High specific activity in place of solid flow restrictor | A.6 |
| A12 | SFR | SFR | Solid flow restrictor | Reference [2]Figure 38 |
| A13 | LSFR | LSFR | Long solid flow restrictor | Reference [2] Figure 38 |
| A14 | LSFR | LSFR | Long solid flow restrictor | Reference [2] Figure 38 |
| A15 | LSFR | LSFR | Long solid flow restrictor | Reference [2] Figure 38 |
| A16 | LSFR | LSFR | Long solid flow restrictor | Reference [2] Figure 38 |
| B1 | YSFR | YSFR | Solid flow restrictor | Reference [2] Figure 40 |
| B2 | YSFR | YSFR | Solid flow restrictor | Reference [2] Figure 40 |
| B3 | YSFR | BHSACO | High specific activity in B position | A.6 |
| B4 | SUS | BHSACO | High specific activity in B position | A.6 |
| B5 | YSFR | BHSACO | High specific activity in B position | A.6 |
| B6 | YSFR | BHSACO | High specific activity in B position | A.6 |
| B7 | YSFR | Hydraulic Shuttle Irradiation System (HSIS) | Rabbit Facility | A.8 |
| B8 | YSFR | YSFR | Solid flow restrictor | Reference [2] Figure 40 |
| B9 | SIBF | SIBF | Small I beryllium filler | Reference [2] Figure 40 |
| B10 | SIBF | SIBF | Small I beryllium filler | Reference [2] Figure 40 |
| B11 | SIBF | SIBF | Small I beryllium filler | Reference [2] Figure 40 |
| B12 | SIBF | AGR2 | Advanced Graphite Reactor-2 Test | A.9 |
| I1 | LIBF | LIBF | Large I beryllium filler | Reference [2] Figure 40 |

Table 1. Experiment loading for Cycle 149B used in the benchmark models [2] [5] [6].

| Position | 94CIC Experiment | Experiment Loading | Comments | Reference/Section Description |
|---|---|---|---|---|
| I2 | MIBF | MIBF | Medium I beryllium filler | Reference [2] Figure 40 |
| I3 | MIBF | MIBF | Medium I beryllium filler | Reference [2] Figure 40 |
| I4 | MIBF | MIBF | Medium I beryllium filler | Reference [2] Figure 40 |
| I5 | MIBF | MIBF | Medium I beryllium filler | Reference [2] Figure 40 |
| I6 | LIBF | LIBF | Large I beryllium filler | Reference [2] Figure 40 |
| I7 | MIBF | MIBF | Medium I beryllium filler | Reference [2] Figure 40 |
| I8 | MIBF | MIBF | Medium I beryllium filler | Reference [2] Figure 40 |
| I9 | MIBF | MIBF | Medium I beryllium filler | Reference [2] Figure 40 |
| I10 | MIBF | MIBF | Medium I beryllium filler | Reference [2] Figure 40 |
| I11 | LIBF | LIBF | Large I beryllium filler | Reference [2] Figure 40 |
| I12 | MIBF | MIBF | Medium I beryllium filler | Reference [2] Figure 40 |
| I13 | MIBF | MIBF | Medium I beryllium filler | Reference [2] Figure 40 |
| I14 | MIBF | MIBF | Medium I beryllium filler | Reference [2] Figure 40 |
| I15 | MIBF | MIBF | Medium I beryllium filler | Reference [2] Figure 40 |
| I16 | LIBF | LIBF | Large I beryllium filler | Reference [2] Figure 40 |
| I17 | MIBF | MIBF | Medium I beryllium filler | Reference [2] Figure 40 |
| I18 | MIBF | MIBF | Medium I beryllium filler | Reference [2] Figure 40 |
| I19 | MIBF | MIBF | Medium I beryllium filler | Reference [2] Figure 40 |
| I20 | MIBF | MIBF | Medium I beryllium filler | Reference [2] Figure 40 |
| I21 | SIBF | SIBF | Small I beryllium filler | Reference [2] Figure 40 |
| I22 | SIBF | SIBF | Small I beryllium filler | Reference [2] Figure 40 |
| I23 | SIBF | SIBF | Small I beryllium filler | Reference [2] Figure 40 |
| I24 | SIBF | SIBF | Small I beryllium filler | Reference [2] Figure 40 |

Table 1. Experiment loading for Cycle 149B used in the benchmark models [2] [5] [6].

| Position | 94CIC Experiment | Experiment Loading | Comments | Reference/Section Description |
|---|---|---|---|---|
| H1 | HLSACCB | HFSHIM | Fixed hafnium shim in place of Low Specific Activity (LSA) cobalt capsules | A.7 |
| H2 | FMWH | HHSACO | High specific activity cobalt | A.6 |
| H3 | HN16 | HN16 | N-16 instrument position | Reference [2] Figure 36 |
| H4 | HLSACCB | HHSACO | High specific activity cobalt in place of LSA cobalt capsules | A.6 |
| H5 | HLSACCB | HFSHIM | Fixed hafnium shim in place of LSA cobalt capsules | A.7 |
| H6 | FMWH | HHSACO | High specific activity cobalt | A.6 |
| H7 | HLSACCB | HHSACO | Fixed hafnium shim in place of LSA cobalt capsules | A.6 |
| H8 | HLSACCB | HHSACO | Fixed hafnium shim in place of LSA cobalt capsules | A.6 |
| H9 | HLSACCB | HFSHIM | Fixed hafnium shim in place of LSA cobalt capsules | A.7 |
| H10 | FMWH | HHSACO | High specific activity cobalt | A.6 |
| H11 | HN16 | HN16 | N-16 instrument position | Reference [2] Figure 36 |
| H12 | HLSACCB | HHSACO | Fixed hafnium shim in place of LSA cobalt capsules | A.6 |
| H13 | HLSACCB | HFSHIM | Fixed hafnium shim in place of LSA cobalt capsules | A.7 |
| H14 | FMWH | HHSACO | Fixed hafnium shim in place of LSA cobalt capsules | A.6 |
| H15 | HLSACCB | HHSACO | Fixed hafnium shim in place of LSA cobalt capsules | A.6 |

Table 1. Experiment loading for Cycle 149B used in the benchmark models [2] [5] [6].

| Position | 94CIC Experiment | Experiment Loading | Comments | Reference/Section Description |
|---|---|---|---|---|
| H16 | HLSACCB | HHSACO | Fixed hafnium shim in place of LSA cobalt capsules | A.6 |

Table 2. Experiment loading for Cycle 150B used in the benchmark models [2] [4] [6].

| Position | 94CIC Experiment | Experiment Loading | Comments | Reference/Section Description |
|---|---|---|---|---|
| SWFT | EmptySIPT | SE100_SW100 | Empty SIPT filled with standard backup | A.2 |
| SEFT | EmptySIPT | SE100_SW100 | Empty SIPT filled with standard backup | A.2 |
| NFT | EmptySIPT | N100 | Empty SIPT filled with standard backup | A.2 |
| WFT | EmptySIPT | N100 | Empty SIPT filled with standard backup | A.2 |
| NEFT | LIHA103 | LIHA103 | Large irradiation housing assembly used during CIC | Reference [2] Figure 35 |
| CFT | CIHA103 | AFIP7 | AFIP-7 Experiment | 3 |
| EFT | SIHA103 | SIHA145 | 149B/150B irradiation contains advanced fuel cycle baskets. | A.5, Reference [2] Figure 37 |
| SFT | SIHA103 | AGC2 | Advanced Graphite-2 experiment. | A.4 |
| NWFT | NWFiller | NW100 | NW-100 is the standard large in-pile | A.3 |

Table 2. Experiment loading for Cycle 150B used in the benchmark models [2] [4] [6].

| Position | 94CIC Experiment | Experiment Loading | Comments | Reference/Section Description |
|---|---|---|---|---|
| | | | tube backup assembly | |
| A1 | SFR | HHSACO | High specific activity in place of solid flow restrictor | A.6 |
| A2 | SFR | HHSACO | High Specific activity in place of solid flow restrictor | A.6 |
| A3 | SFR | SFR | Solid flow restrictor | [2] Figure 38 |
| A4 | SFR | HHSACO | High specific activity in place of solid flow restrictor | A.6 |
| A5 | SFR | HHSACO | High specific activity in place of solid flow restrictor | A.6 |
| A6 | SFR | HHSACO | High specific activity in place of solid flow restrictor | A.6 |
| A7 | SFR | HHSACO | High specific activity in place of solid flow restrictor | A.6 |
| A8 | SFR | HHSACO | High specific activity in place of | A.6 |

Table 2. Experiment loading for Cycle 150B used in the benchmark models [2] [4] [6].

| Position | 94CIC Experiment | Experiment Loading | Comments | Reference/Section Description |
|---|---|---|---|---|
| | | | solid flow restrictor | |
| A9 | SFR | HHSACO | High specific activity in place of solid flow restrictor | A.6 |
| A10 | SFR | AFC3 | High specific activity in place of solid flow restrictor | A.6 |
| A11 | SFR | AFC3 | High specific activity in place of solid flow restrictor | A.6 |
| A12 | SFR | SFR | Solid flow restrictor | Reference [2] Figure 38 |
| A13 | LSFR | LSFR | Long solid flow restrictor | Reference [2] Figure 38 |
| A14 | LSFR | LSFR | Long solid flow restrictor | Reference [2] Figure 38 |
| A15 | LSFR | LSFR | Long solid flow restrictor | Reference [2] Figure 38 |
| A16 | LSFR | LSFR | Long solid flow restrictor | Reference [2] Figure 38 |
| B1 | YSFR | YSFR | Solid flow restrictor | Reference [2] Figure 40 |
| B2 | YSFR | YSFR | Solid flow restrictor | Reference [2] Figure 40 |
| B3 | YSFR | BHSACO | High specific activity in B position | A.6 |

Table 2. Experiment loading for Cycle 150B used in the benchmark models [2] [4] [6].

| Position | 94CIC Experiment | Experiment Loading | Comments | Reference/Section Description |
|---|---|---|---|---|
| B4 | SUS | BHSACO | High specific activity in B position | A.6 |
| B5 | YSFR | BHSACO | High specific activity in B position | A.6 |
| B6 | YSFR | BHSACO | High specific activity in B position | A.6 |
| B7 | YSFR | HSIS | Rabbit Facility | A.8 |
| B8 | YSFR | YSFR | Solid flow restrictor | Reference [2] Figure 40 |
| B9 | SIBF | RERTR-12 | RERTR-12 Experiment | A.10 |
| B10 | SIBF | SIALF | Small I beryllium filler | A.12 |
| B11 | SIBF | SIALF | Small I beryllium filler | A.12 |
| B12 | SIBF | AGR2 | Advanced Graphite Reactor-2 Test | A.9 |
| I1 | LIBF | LIBF | Large I beryllium filler | Reference [2] Figure 40 |
| I2 | MIBF | MIBF | Medium I beryllium filler | Reference [2] Figure 40 |
| I3 | MIBF | MIBF | Medium I beryllium filler | Reference [2] Figure 40 |
| I4 | MIBF | MIBF | Medium I beryllium filler | Reference [2] Figure 40 |
| I5 | MIBF | MIBF | Medium I beryllium filler | Reference [2] Figure 40 |

Table 2. Experiment loading for Cycle 150B used in the benchmark models [2] [4] [6].

| Position | 94CIC Experiment | Experiment Loading | Comments | Reference/Section Description |
|---|---|---|---|---|
| I6 | LIBF | LIBF | Large I beryllium filler | Reference [2] Figure 40 |
| I7 | MIBF | MIBF | Medium I beryllium filler | Reference [2] Figure 40 |
| I8 | MIBF | MIBF | Medium I beryllium filler | Reference [2] Figure 40 |
| I9 | MIBF | MIBF | Medium I beryllium filler | Reference [2] Figure 40 |
| I10 | MIBF | MIBF | Medium I beryllium filler | Reference [2] Figure 40 |
| I11 | LIBF | LIBF | Large I beryllium filler | Reference [2] Figure 40 |
| I12 | MIBF | MIBF | Medium I beryllium filler | Reference [2] Figure 40 |
| I13 | MIBF | MIBF | Medium I beryllium filler | Reference [2] Figure 40 |
| I14 | MIBF | MIBF | Medium I beryllium filler | Reference [2] Figure 40 |
| I15 | MIBF | MIBF | Medium I beryllium filler | Reference [2] Figure 40 |
| I16 | LIBF | LIBF | Large I beryllium filler | Reference [2] Figure 40 |
| I17 | MIBF | MIBF | Medium I beryllium filler | Reference [2] Figure 40 |
| I18 | MIBF | MIBF | Medium I beryllium filler | Reference [2] Figure 40 |
| I19 | MIBF | MIBF | Medium I beryllium filler | Reference [2] Figure 40 |

Table 2. Experiment loading for Cycle 150B used in the benchmark models [2] [4] [6].

| Position | 94CIC Experiment | Experiment Loading | Comments | Reference/Section Description |
|---|---|---|---|---|
| I20 | MIBF | MIBF | Medium I beryllium filler | Reference [2] Figure 40 |
| I21 | SIBF | SIALF | Small I aluminum filler | A.12 |
| I22 | SIBF | SIALF | Small I aluminum filler | A.12 |
| I23 | SIBF | SIALF | Small I aluminum filler | A.12 |
| I24 | SIBF | SIALF | Small I aluminum filler | A.12 |
| H1 | HLSACCB | HFSHIM | Fixed hafnium shim in place of LSA cobalt capsules | A.7 |
| H2 | FMWH | HHSACO | High specific activity cobalt | A.6 |
| H3 | HN16 | HN16 | N-16 instrument position | Reference [2] Figure 36 |
| H4 | HLSACCB | HHSACO | High specific activity cobalt in place of LSA cobalt capsules | A.6 |
| H5 | HLSACCB | HFSHIM | Fixed hafnium shim in place of LSA cobalt capsules | A.7 |
| H6 | FMWH | HHSACO | High specific | A.6 |

Table 2. Experiment loading for Cycle 150B used in the benchmark models [2] [4] [6].

| Position | 94CIC Experiment | Experiment Loading | Comments | Reference/Section Description |
|---|---|---|---|---|
| | | | activity cobalt | |
| H7 | HLSACCB | HHSACO | Fixed hafnium shim in place of LSA cobalt capsules | A.6 |
| H8 | HLSACCB | HHSACO | Fixed hafnium shim in place of LSA cobalt capsules | A.6 |
| H9 | HLSACCB | HFSHIM | Fixed hafnium shim in place of LSA cobalt capsules | A.7 |
| H10 | FMWH | HHSACO | High specific activity cobalt | A.6 |
| H11 | HN16 | HN16 | N-16 instrument position | Reference [2] Figure 36 |
| H12 | HLSACCB | HHSACO | Fixed hafnium shim in place of LSA cobalt capsules | A.6 |
| H13 | HLSACCB | HFSHIM | Fixed hafnium shim in place of LSA cobalt capsules | A.7 |
| H14 | FMWH | HHSACO | Fixed hafnium shim in place of LSA cobalt capsules | A.6 |

Table 2. Experiment loading for Cycle 150B used in the benchmark models [2] [4] [6].

| Position | 94CIC Experiment | Experiment Loading | Comments | Reference/Section Description |
|---|---|---|---|---|
| H15 | HLSACCB | HHSACO | Fixed hafnium shim in place of LSA cobalt capsules | A.6 |
| H16 | HLSACCB | HHSACO | Fixed hafnium shim in place of LSA cobalt capsules | A.6 |

# 3. AFIP-7 EXPERIMENT

In this analysis, the model of the AFIP-7 experiment in the center flux trap is important [6]. The INL drawings used to model the AFIP-7 experiment are listed in Table 3. The following subsection describes the fuel plate data for AFIP-7.

Table 3. AFIP-7 drawings used to model the AFIP-7 experiment.

| INL Drawing | Drawing Title |
|---|---|
| 602649 | ATR AFIP-7 Experiment Element Holder Assembly |
| 602648 | ATR AFIP-7 Experimental Element Fuel Plate Assembly |
| 602647 | ATR AFIP-7 Experimental Element Fuel Element Assembly and Details |
| 602646 | ATR AFIP-7 Experimental Element Final Assembly |
| 602645 | ATR AFIP-7 In-Vessel Installation |
| 602650 | ATR AFIP-7 Experimental Holder Details |
| 602689 | ATR AFIP-7 Hf Rod Detail |
| 602688 | ATR AFIP-7 Hf Rod Assembly |
| 602687 | ATR AFIP-7 Hf Rod Basket Assembly |

## 3.1 Fuel Plate Data

The AFIP-7 experiment was modeled from data in Reference [6]. The fuel matrix is composed of U-10Mo at 19.75 wt% U-235 enrichment. A summary of each fuel plate's compositions is listed in Table 4. The fuel core thickness is nominally 0.013 inches. Each plate has a nominal 0.001-inch thick zirconium interlayer between the two largest surfaces of the fuel core and the aluminum cladding. The active fuel length of each plate is nominally 38.5 inches long. The zirconium is transparent to neutrons and therefore has been neglected in the model. The fuel plates are also modeled with nominal conditions; however, the as-built density of each plate is maintained.

With respect to the AFIP-7 model, each plate fuel zone is modeled with 10 azimuthal regions and 77 axial regions. The model is intended to provide sufficient detail to compare PIE results to the burnup calculations for the fuel core. The plates are placed in an aluminum holder with a spacing of 0.166 inches (0.42164 cm).

The AFIP-7 plates are held in place by aluminum rails. The rails are 45.76 inches long (116.2304 cm), which is nearly the active length of the ATR core. On each side of the plates, a block of aluminum is modeled with a rectangular shape of 0.187 x 0.697 inches (0.4675 cm x 1.77038 cm). The width of the rails, when assembled with fuel plates, is 2.643 inches (6.71322 cm).

## 3.2 AFIP-7 Holder

The AFIP-7 holder is constructed of a 3.125 inches (7.9375 cm) diameter aluminum cylinder and is assumed to run the entire length of the model. The holder has an opening in the center cut out to support the AFIP-7 fuel plates. The cutout opening has a width of 2.723 inches (6.1942 cm). The curves on the top and bottom have a radius of 3.607 and 3.557 inches (9.16178 and 9.03478 cm). The two curves intersect horizontal planes at ±0.3885 inches (±0.98679 cm). On the outside of the holder, the sides were shaved down to allow for coolant flow in the event of a handling accident. These are referred to here as cutouts, which are on each side of the holder. The cutouts are bounded by the outer radius of the holder and vertical planes at ±2.723 inches (6.1942 cm). There are four cutouts with a length of 5.145 inches (13.0683 cm), 8.770 inches (22.2758 cm), 8.770 inches (22.2758 cm), and 4.395 inches (11.1633 cm) from bottom to top. The bottom elevation of the four cutouts is −18.198 inches, −10.198 inches (25.90292 cm), 1.427 inches (3.62458 cm), and 13.052 inches (33.15208 cm) relative to core mid-plane. A diagram of the AFIP-7 experiment with holder is shown in Figure 1 and Figure 2. Drawings used to support the modeling of the AFIP-7 experiment are listed in Table 3.

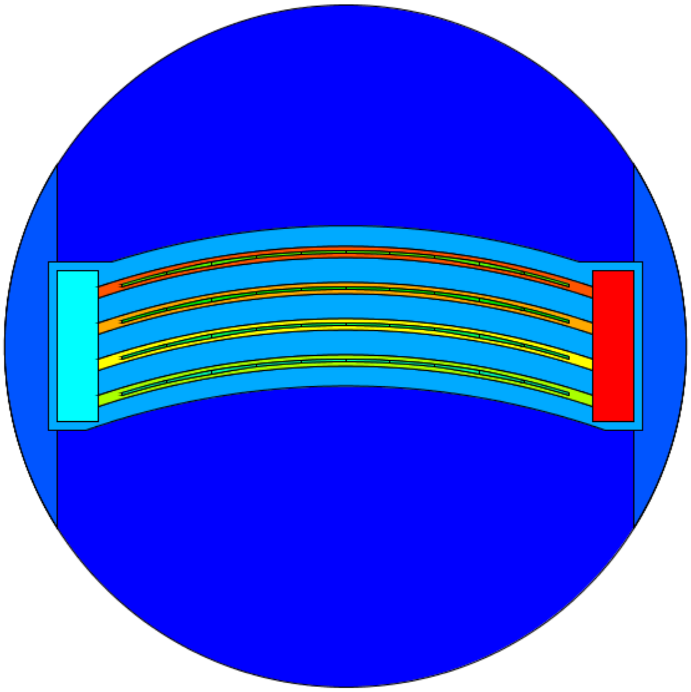

Figure 1. Cross section of the AFIP-7 LEU experiment.

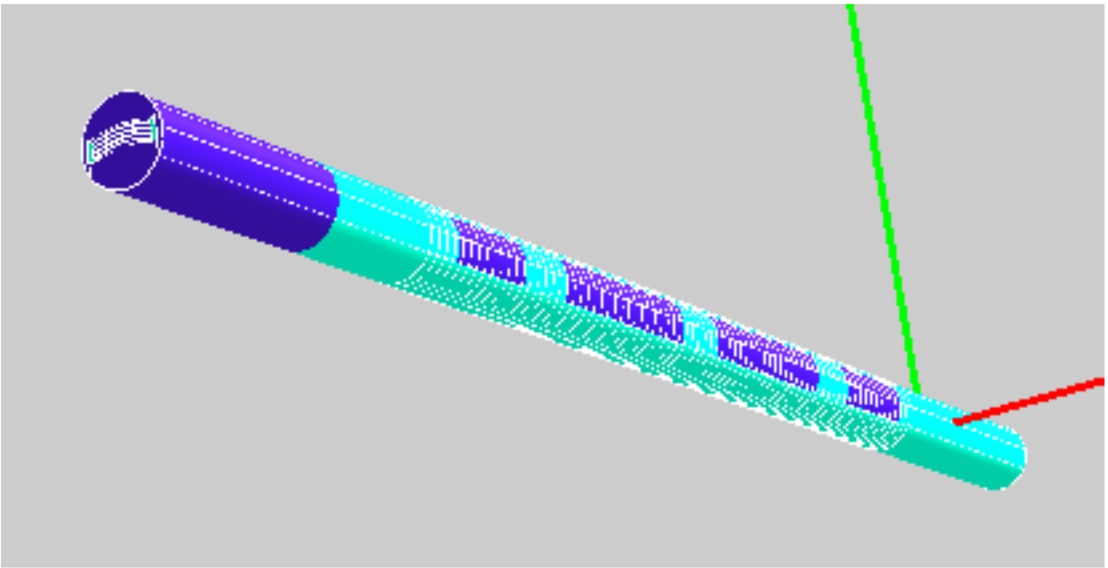

Figure 2. Isometric view of the AFIP-7 experiment.

Table 4. Fuel plate constituent masses (as-built) for AFIP-7 [6].

| | | Fuel Phase Constituent Masses (g) | | | | Interlayer Phase Mass (g) | Cladding Mass (g) |
|---|---|---|---|---|---|---|---|
| Plate ID | Fuel Plate Mass (g) | U-Mo Fuel Phase Total | Total U | U-235 | Mo | Zr | Al-6061 |
| 7ZH-1 | 479.21 | 283.07 | 251.81 | 49.26 | 31.26 | 19.23 | 176.91 |
| 7ZH-2 | 500.26 | 314.03 | 283.71 | 56.13 | 30.32 | 14.11 | 172.12 |
| 7ZH-3 | 492.00 | 304.57 | 271.48 | 53.97 | 33.09 | 15.66 | 171.77 |
| 7ZH-4 | 503.71 | 313.95 | 283.64 | 56.11 | 30.31 | 14.10 | 175.66 |
| Total | 1975.18 | 1215.62 | 1090.64 | 215.46 | 124.98 | 63.10 | 696.46 |

Table 5. Calculated atom densities for the AFIP-7 fuel plates.

| Plate ID | Fuel Plate Mass (g) | Fuel Core Thickness (cm) | Fuel Core Volume (cc) | U-238 (atoms/cm-b) | U-235(atoms/cm-b) | Mo (atoms/cm-b) | Total |
|---|---|---|---|---|---|---|---|
| 7ZH-1 | 479.21 | 0.033 | 17.672 | 2.8996E-02 | 7.1419E-03 | 1.1103E-02 | 4.7241E-02 |
| 7ZH-2 | 500.26 | 0.033 | 17.996 | 3.1992E-02 | 7.9915E-03 | 1.0575E-02 | 5.0559E-02 |
| 7ZH-3 | 492 | 0.033 | 17.866 | 3.0798E-02 | 7.7395E-03 | 1.1625E-02 | 5.0162E-02 |
| 7ZH-4 | 503.71 | 0.033 | 17.971 | 3.2030E-02 | 7.9997E-03 | 1.0587E-02 | 5.0616E-02 |

# 4. ATR OPERATING CONDITIONS

## 4.1 ATR Fuel Loading

The ATR fuel loading is based on the ATR MC21 fuel database. The fuel database was created by performing core follow calculations beginning with ATR Cycle 144B. At the end of the ATR operating cycle simulation, the fuel element composition files from MC21 are saved for later use. The database also maintains the time at which the shutdown occurred for each element. Prior to building the ATR cycle model for 149B and 150B, the fuel elements were decayed from the shutdown time to startup time. The ATR fuel element loading for Cycles 149B and 150B are presented in Table 6 and

Table 7. The element loading identification numbers were taken from References [5] and [4]. However, the gram loading listed in the Tables below will vary slightly due to the use of the MC21 fuel database. The values documented in the Reference documents were generated from the PDQ database, which is a two-dimensional diffusion code. There are several elements that were last irradiated before Cycle 144B. In the case of these elements, the gram loading was taken from the PDQ database, though a generic element database was used that incorporated a best estimate of the compositions based on fuel loading. Those elements are identified in the following tables.

In order to support future benchmarking activities the fuel compositions in atom densities are saved in a spreadsheet and included for supporting information. The fuel spreadsheet is titled “149B_150B_Fuel_Loading.xlsx.” Compositions are condensed from the MC21 model to 12 axial regions per fuel plate for 9120 regions total per core (40 elements x 19 plates x 12 axial regions).

Table 6. Core loading for Cycle 149B [5].

| Position | Element ID | $^{235}$U (g) | $^{10}$B (g) | Accumulated Lobe Exposure (MWd) |
|---|---|---|---|---|
| 1 | XA343T* | 800.80 | 0.13 | 1568 |
| 2 | XA779TNB | 1075.00 | 0.00 | 0 |
| 3 | XA931T | 1075.00 | 0.66 | 0 |
| 4 | XA782TNB | 1075.00 | 0.00 | 0 |
| 5 | XA875T | 941.26 | 0.28 | 856 |
| 6 | XA878T | 941.16 | 0.28 | 856 |
| 7 | XA831T | 1075.00 | 0.66 | 0 |
| 8 | XA861T | 1075.00 | 0.66 | 0 |
| 9 | YA553TM | 896.65 | 0.22 | 1020 |
| 10 | YA547TM | 760.87 | 0.09 | 1884 |
| 11 | XA735T* | 836.45 | 0.15 | 1544 |
| 12 | XA925T | 1075.00 | 0.66 | 0 |
| 13 | XA924T | 1075.00 | 0.66 | 0 |
| 14 | XA876T | 971.93 | 0.34 | 856 |
| 15 | XA872T | 900.33 | 0.20 | 1094 |
| 16 | XA633TNB | 911.69 | 0.00 | 856 |
| 17 | XA929T | 1075.00 | 0.66 | 0 |
| 18 | XA940T | 1075.00 | 0.66 | 0 |
| 19 | XA930T | 1075.00 | 0.66 | 0 |
| 20 | XA698T* | 836.45 | 0.15 | 1299 |
| 21 | XA729T* | 838.80 | 0.13 | 1223 |
| 22 | XA816T | 1075.00 | 0.66 | 0 |
| 23 | XA927T | 1075.00 | 0.66 | 0 |
| 24 | XA945T | 1075.00 | 0.66 | 0 |
| 25 | XA630TNB | 907.32 | 0.00 | 904 |
| 26 | XA883T | 900.61 | 0.20 | 1021 |
| 27 | XA928T | 1075.00 | 0.66 | 0 |
| 28 | XA935T | 1075.00 | 0.66 | 0 |
| 29 | XA867T | 896.95 | 0.21 | 903 |
| 30 | XA733T* | 849.61 | 0.15 | 1544 |
| 31 | XA835T | 822.51 | 0.13 | 1408 |
| 32 | XA905T | 903.51 | 0.22 | 904 |
| 33 | XA778TNB | 1075.00 | 0.00 | 0 |
| 34 | XA607TNB | 899.93 | 0.00 | 907 |

Table 6. Core loading for Cycle 149B [5].

| Position | Element ID | $^{235}$U (g) | $^{10}$B (g) | **Accumulated Lobe Exposure (MWd)** |
|---|---|---|---|---|
| 35 | XA864T | 941.52 | 0.29 | 707 |
| 36 | XA897T | 895.87 | 0.20 | 1157 |
| 37 | XA895T | 871.21 | 0.17 | 1157 |
| 38 | XA784TNB | 1075.00 | 0.00 | 0 |
| 39 | XA593TNB* | 909.57 | 0.00 | 883 |
| 40 | YA443TM* | 810.71 | 0.12 | 1454 |
| Total | | 38520 | 12 | -- |
| *Elements last irradiated in cycles prior to 144B. | | | | |

Table 7. ATR fuel element core load for Cycle 150B [4].

| Position | Element ID | $^{235}$U (g) | $^{10}$B (g) | Accumulated Lobe Exposure (MWd) |
|---|---|---|---|---|
| 1 | XA132T* | 789.73 | 0.12 | 1659 |
| 2 | XA926T | 1075.00 | 0.66 | 0 |
| 3 | XA932T | 1075.00 | 0.66 | 0 |
| 4 | XA228T | 963.91 | 0.32 | 927 |
| 5 | XA764TNB | 944.83 | 0.00 | 663 |
| 6 | XA892T | 973.13 | 0.34 | 663 |
| 7 | XA939T | 1075.00 | 0.66 | 0 |
| 8 | XA938T | 1075.00 | 0.66 | 0 |
| 9 | XA783TNB | 1075.00 | 0.00 | 0 |
| 10 | YA497TM* | 721.92 | 0.07 | 1777 |
| 11 | XA820T | 798.31 | 0.11 | 2169 |
| 12 | XA941T | 1075.00 | 0.66 | 0 |
| 13 | XA942T | 1075.00 | 0.66 | 0 |
| 14 | XA943T | 1075.00 | 0.66 | 0 |
| 15 | XA911T | 926.59 | 0.24 | 847 |
| 16 | XA920T | 925.39 | 0.24 | 883 |
| 17 | XA944T | 1075.00 | 0.66 | 0 |
| 18 | XA946T | 1075.00 | 0.66 | 0 |
| 19 | XA957T | 1075.00 | 0.66 | 0 |
| 20 | YA476TM | 771.75 | 0.09 | 1828 |
| 21 | XA856T | 838.51 | 0.14 | 1300 |
| 22 | XA958T | 1075.00 | 0.66 | 0 |
| 23 | XA959T | 1075.00 | 0.66 | 0 |
| 24 | XA960T | 1075.00 | 0.66 | 0 |
| 25 | XA916T | 909.67 | 0.23 | 847 |
| 26 | XA919T | 908.53 | 0.21 | 883 |
| 27 | XA961T | 1075.00 | 0.66 | 0 |
| 28 | XA962T | 1075.00 | 0.66 | 0 |
| 29 | XA963T | 1075.00 | 0.66 | 0 |
| 30 | YA552TM | 768.28 | 0.09 | 1923 |
| 31 | XA881T | 790.46 | 0.10 | 1739 |
| 32 | XA780TNB | 1075.00 | 0.00 | 0 |
| 33 | XA915T | 914.13 | 0.22 | 847 |
| 34 | XA871T | 888.23 | 0.19 | 1021 |
| 35 | XA758TNB | 902.95 | 0.00 | 1020 |

| Position | Element ID | $^{235}U$ (g) | $^{10}B$ (g) | Accumulated Lobe Exposure (MWd) |
|---|---|---|---|---|
| 36 | XA825T | 862.66 | 0.17 | 1191 |
| 37 | XA229T | 932.39 | 0.26 | 927 |
| 38 | XA923T | 912.12 | 0.23 | 883 |
| 39 | XA781TNB | 1075.00 | 0.00 | 0 |
| 40 | XA846T | 801.09 | 0.11 | 2092 |
| Total | | 38669 | 14 | |
| *Elements last irradiated in cycles prior to 144B. | | | | |

The ATR Outer Shim Control Cylinder (OSCC) and neckshim positions were modeled as reported from the ATR operating history. During the depletion simulation, the shims were adjusted to match actual operating conditions at the time of each transport calculation. A summary of the operating positions for the OSCCs and neckshims are reported in Table 8 through Table 11.

Table 8. ATR OSCC positions for Cycle 149B (degrees of rotation).

| Time | Date | NW | NE | SW | SE |
|---|---|---|---|---|---|
| 1200 | 6/6/11 | 38.7 | 38.7 | 38.85 | 38.6 |
| 1200 | 6/6/11 | 38.7 | 38.7 | 38.85 | 38.6 |
| 1200 | 6/6/11 | 38.7 | 38.7 | 38.85 | 38.6 |
| 1500 | 6/6/11 | 40.7 | 40.45 | 40.55 | 40.4 |
| 2200 | 6/6/11 | 48.1 | 59.5 | 52.25 | 56.75 |
| 300 | 6/7/11 | 56 | 68.6 | 58.6 | 63.7 |
| 1000 | 6/7/11 | 66.95 | 80 | 68.6 | 72.4 |
| 1500 | 6/7/11 | 71.45 | 85.6 | 72.75 | 78 |
| 1500 | 6/8/11 | 75.85 | 92.45 | 78.3 | 83.65 |
| 1500 | 6/9/11 | 75.4 | 94.7 | 79 | 85.1 |
| 1500 | 6/10/11 | 77.05 | 96.5 | 79.5 | 85.45 |
| 1500 | 6/17/11 | 79.8 | 91.8 | 82.8 | 88.1 |
| 1500 | 6/24/11 | 82.8 | 83.95 | 84.85 | 84.7 |
| 1500 | 7/1/11 | 85.8 | 82.8 | 83.6 | 83.1 |
| 1500 | 7/8/11 | 86 | 87.55 | 84.6 | 88 |
| 1459 | 7/15/11 | 85.5 | 83.5 | 87 | 84.9 |
| 1459 | 7/22/11 | 82.3 | 85.1 | 82.5 | 87.3 |
| 1459 | 7/29/11 | 93 | 97.5 | 96.5 | 101.5 |
| 959 | 7/30/11 | 93.6 | 98.2 | 97.2 | 102.45 |

Table 9. ATR Neckshim positions for Cycle 149B (I = inserted, O = Withdrawn, R = Regulating Rod; neckshims are ordered 1–6 in each column of the table).

| Time | Date | NW (NS 1–6) | NE (NS 1–6) | SW (NS 1–6) | SE (NS 1–6) |
|---|---|---|---|---|---|
| 1200 | 6/6/11 | IIIIII | IIIIII | IIIRII | IIIRII |
| 1200 | 6/6/11 | IIIIII | IIIIII | IIIRII | IIIRII |
| 1200 | 6/6/11 | IIIIII | IIIIII | IIIRII | IIIRII |
| 1500 | 6/6/11 | IIIIII | IIIIII | IIIRII | IIIRII |
| 2200 | 6/6/11 | IIIIII | IIIIII | IIIRII | IIIRII |
| 300 | 6/7/11 | IIIIII | IIIIII | IIIRII | IIIRII |
| 1000 | 6/7/11 | IIIIII | IIIIII | IIIRII | IIIRII |
| 1500 | 6/7/11 | IIIIII | IIIIII | IIIRII | IIIRII |
| 1500 | 6/8/11 | IIIIII | IIIIII | IIIRII | IIIRII |
| 1500 | 6/9/11 | IIIIII | IIIIII | IIIRII | IIIRII |
| 1500 | 6/10/11 | IIIIII | IIIIII | IIIRII | IIIRII |
| 1500 | 6/17/11 | IIIIII | IIIIOO | IIIRII | IIIRII |
| 1500 | 6/24/11 | IIIIII | IIOOOO | IIIRII | IIIRIO |
| 1500 | 7/1/11 | IIIIII | IOOOOO | IIIRIO | IIIROO |
| 1500 | 7/8/11 | IIIIIO | IOOOOO | IIIROO | IIIROO |
| 1459 | 7/15/11 | IIIIOO | OOOOOO | IIIROO | OOOROO |
| 1459 | 7/22/11 | IOOIOO | OOOOOO | OOOROO | OOOROO |
| 1459 | 7/29/11 | OOOIOO | OOOOOO | OOOROO | OOOROO |
| 959 | 7/30/11 | OOOIOO | OOOOOO | OOOROO | OOOROO |

Table 10. ATR OSCC positions for Cycle 150B (degrees of rotation).

| Time | Date | NW | NE | SW | SE |
|---|---|---|---|---|---|
| 0 | 10/15/11 | 41.2 | 41.15 | 41.3 | 41.3 |
| 900 | 10/15/11 | 50.75 | 50.9 | 51.05 | 50.8 |
| 1459 | 10/15/11 | 55.3 | 60.55 | 63.25 | 60.7 |
| 1800 | 10/15/11 | 58.75 | 65.15 | 67.3 | 65.15 |
| 1800 | 10/16/11 | 82.8 | 90.95 | 95.45 | 92.7 |
| 1800 | 10/17/11 | 94.8 | 87.1 | 88.2 | 91.75 |
| 1800 | 10/18/11 | 83.4 | 83.6 | 86.1 | 89.1 |
| 1800 | 10/25/11 | 86.85 | 82.3 | 87 | 85.5 |
| 1759 | 11/1/11 | 89.5 | 84.1 | 85.2 | 86.05 |
| 1759 | 11/8/11 | 96.9 | 89.15 | 90.55 | 91.6 |
| 1759 | 11/15/11 | 95.2 | 85.9 | 83.85 | 85 |
| 1759 | 11/22/11 | 106.2 | 87.4 | 92.05 | 87.5 |
| 959 | 11/26/11 | 113.55 | 88.6 | 96 | 91.8 |

Table 11. ATR Neckshim positions for Cycle 150B (I = inserted, O = Withdrawn, R = Regulating Rod; neckshims are ordered 1–6 in each column of the table).

| Time | Date | NW (NS 1–6) | NE (NS 1–6) | SW (NS 1–6) | SE (NS 1–6) |
|---|---|---|---|---|---|
| 0 | 10/15/11 | IIIIII | IIIIII | IIIRII | IIIRII |
| 900 | 10/15/11 | IIIIII | IIIIII | IIIRII | IIIRII |
| 1459 | 10/15/11 | IIIIII | IIIIII | IIIRII | IIIRII |
| 1800 | 10/15/11 | IIIIII | IIIIII | IIIRII | IIIRII |
| 1800 | 10/16/11 | IIIIII | IIIIIO | IIIRII | IIIRII |
| 1800 | 10/17/11 | IIIIII | IIIIIO | IIIRIO | IIIRII |
| 1800 | 10/18/11 | IIIIOO | IIIIIO | IIIRIO | IIIRII |
| 1800 | 10/25/11 | IIOIOO | IIIIOO | IIIRIO | IIIRIO |
| 1759 | 11/1/11 | IOOIOO | IIIIOO | IIIROO | IIIRIO |
| 1759 | 11/8/11 | OOOIOO | IIIIOO | IIIROO | IIIRIO |
| 1759 | 11/15/11 | OOOIOO | IIIOOO | OOOROO | IIIROO |
| 1759 | 11/22/11 | OOOIOO | IIOOOO | OOOROO | IIOROO |
| 959 | 11/26/11 | OOOIOO | IOOOOO | OOOROO | IIOROO |

## 4.2 Power History

The ATR operating history data is used in the simulation analysis. ATR is operated by establishing the lobe power split and maintaining planned reactor power in each of the four corner lobes, which can be controlled and maintained by the OSCCs. The ATR constrained operating power for Cycle 149B and 150B are listed in Table 12 and Table 13.

Table 12. ATR operating powers for Cycle 149B (power in MW).

| Date | Time | NW | NE | C | SW | SE | Total |
|---|---|---|---|---|---|---|---|
| 6/6/11 | 1500 | 6.21 | 5.82 | 9.26 | 7.65 | 7.33 | 36.27 |
| 6/6/11 | 2200 | 12.7 | 12.66 | 18.87 | 16.29 | 16.25 | 76.77 |
| 6/7/11 | 300 | 17.95 | 17.93 | 25.53 | 23.10 | 22.98 | 107.49 |
| 6/7/11 | 1000 | 18.03 | 18.01 | 24.44 | 23.04 | 22.93 | 106.45 |
| 6/7/11 | 1500 | 18.26 | 18.17 | 23.96 | 23.38 | 23.28 | 107.05 |
| 6/8/11 | 1500 | 18.07 | 18.30 | 24.35 | 22.99 | 23.08 | 106.79 |
| 6/9/11 | 1500 | 17.95 | 17.80 | 24.04 | 22.83 | 23.01 | 105.63 |
| 6/10/11 | 1500 | 18.01 | 18.04 | 23.57 | 22.89 | 22.88 | 105.39 |
| 6/17/11 | 1500 | 18.04 | 18.03 | 23.05 | 23.10 | 23.12 | 105.34 |
| 6/24/11 | 1500 | 18.04 | 17.98 | 24.06 | 23.09 | 22.93 | 106.10 |
| 7/1/11 | 1500 | 17.99 | 18.12 | 24.02 | 23.07 | 23.14 | 106.34 |
| 7/8/11 | 1500 | 18.03 | 18.12 | 23.97 | 23.15 | 23.03 | 106.30 |
| 7/15/11 | 1459 | 18.01 | 18.01 | 24.85 | 22.92 | 22.88 | 106.67 |
| 7/22/11 | 1459 | 18.03 | 18.00 | 25.46 | 23.01 | 22.96 | 107.46 |
| 7/29/11 | 1459 | 18.13 | 18.06 | 24.5 | 23.14 | 22.88 | 106.71 |

| Date | Time | NW | NE | C | SW | SE | Total |
|---|---|---|---|---|---|---|---|
| 7/30/11 | 959 | 18.06 | 18.09 | 24.57 | 23.11 | 23.12 | 106.95 |

Table 13. ATR operating powers for Cycle 150B (power in MW).

| Date | Time | NW | NE | C | SW | SE | Total |
|---|---|---|---|---|---|---|---|
| 10/15/11 | 900 | 0.58 | 0.55 | 0.84 | 0.69 | 0.68 | 3.34 |
| 10/15/11 | 1459 | 8.72 | 8.66 | 12.83 | 11.06 | 11.19 | 52.46 |
| 10/15/11 | 1800 | 18.09 | 18.17 | 25.67 | 23.06 | 23.14 | 108.13 |
| 10/16/11 | 1800 | 17.98 | 17.96 | 22.99 | 23.08 | 23.08 | 105.09 |
| 10/17/11 | 1800 | 20.14 | 18.06 | 23.53 | 22.81 | 23.09 | 107.63 |
| 10/18/11 | 1800 | 19.76 | 17.84 | 24.00 | 22.82 | 22.94 | 107.36 |
| 10/25/11 | 1800 | 19.95 | 17.95 | 24.25 | 22.95 | 23.09 | 108.19 |
| 11/1/11 | 1759 | 19.96 | 18.01 | 24.18 | 23.09 | 22.92 | 108.16 |
| 11/8/11 | 1759 | 19.82 | 17.93 | 23.59 | 22.92 | 23.03 | 107.29 |
| 11/15/11 | 1759 | 19.98 | 18.11 | 24.71 | 23.10 | 23.30 | 109.20 |
| 11/22/11 | 1759 | 19.95 | 18.07 | 24.42 | 23.05 | 22.95 | 108.44 |
| 11/26/11 | 959 | 20.02 | 17.94 | 24.11 | 23.04 | 23.05 | 108.16 |

# 5. DISCUSSION/ANALYSIS

## 5.1 Cross-Section Data

The analysis presented in this report was performed with the Evaluated Nuclear Data File (ENDF) Version VIII library (ENDF/B-VIII.0). The data presented in the main body of this report was performed using a standard cross-section library at 273 K. It is recongnized that the fuel temperature is at an elevated temperature, in which Doppler broadening of the cross-sections could have an impact on burnup. As a result, an additional simulation was performed using 373 K cross-sections. Thermal feedback capability has not been implemented into the MC21 ATR model. The water temperatures and densities used in the model are based on inlet reactor operating conditions of 373 psig and 110°F. The elevated temperature value provides a bounding maximum temperature for the experiment. The fission density results for the elevated temperatures are presented in Appendix B.

## 5.2 MC21 Neutron Flux Calculations

The MC21 flux tally has units of neutrons-cm per source neutron. The MC21 flux tally results are used to generate neutron flux input values for the AFIP-7 experiment. The neutron flux conversion factor (NFCF) is defined by Equation (1) but is calculated explicitly in MC21 based on isotopes. Both the $\nu$ and Q-values are calculated from the ENDF libraries in MC21. It should be noted that flux results must also be divided by the volume of cell. MC21 does not divide the neutron flux by the volume.

$$NFCF = \left(\frac{\nu\, fission\ neutrons}{fission}\right)\left(\frac{fission}{\mathrm{Q}\ MeV}\right)\left(\frac{6.24151 \times 10^{18} MeV}{MW_{core\ power} - s}\right)\frac{1}{k_{eff}}$$

(1)

The neutron flux values are calculated using the MC21 flux tally results, the NFCF, and the ATR core power. The neutron flux is calculated using Equation (2).

$$\phi_{neutron} = \left(flux\ tally\, \frac{neutrons{-}cm}{fission\ neutron}\right)\left(\mathrm{NFCF}\ \frac{fission\ neutrons}{Core\ Power\ MW}\right)(Core\ Power\ MW) \quad (2)$$

## 5.3 MC21 Heating Calculations

MC21 reports tally results normalized per source particle. The MC21 energy deposition tally results are used to calculate heat generation rates. MC21 heating tallies have units of eV per source particle (per fission neutron for fission heating or neutron). The heating normalization factor (HNF) is defined by Equation (3).

$$HNF = \left(\frac{\nu\, fission\ neutrons}{fission}\right)\left(\frac{fission}{Q\ MeV}\right)\left(\frac{1{\times}10^{6} W}{MW}\right)\left(\frac{1\ MeV}{1{\times}10^{6}\ eV}\right)\left(\frac{1}{k_{eff}}\right)$$

(3)

The heat generation rate values are calculated using the MC21 tally results, the HNF, and the ATR core power. The prompt heating rates are calculated using Equation (4).

$$PHR = \left(tally\, \frac{eV}{fission\ neutron}\right)\left(HNF\ \frac{fission\ neutrons}{Core\ Power\ MW}\right)(Core\ Power\ MW)$$

(4)

## 5.4 MC21 Depletion Methodology

The depletion of U-235 is calculated using initial U-235 atom densities (AD) for the fuel compositions as well as results of the burnup evaluations for the fuel compositions. The % depletion of U-235 at the end of irradiation is calculated using Equation (5).

$$\%\ Depletion\ U235 = \frac{AD\ U235_{initial} - AD\ U235_{final}}{AD\ U235_{initial}} \times 100 \quad (5)$$

The fission density is calculated by determining the difference in actinide AD at each time step. The fission density is therefore determined by the following equation:

$$Fission\ Density = AD\ Actinides_{Initial} - AD\ Actinides_{final} \quad (6)$$

During PIE, it is not possible to directly measure the U-235 burnup as described by Equation (6). The PIE process involves taking samples from the plates at various locations and using chemical analysis to look at the quantities of U-235, U-238, U-236, and Pu. Since the samples contain cladding, it is not possible to know the exact quantity of initial and final density of U-235 in the fuel core; therefore, U-235 burnup following PIE is provided by Equation (7). The U-235 burnup based on this equation is determined using the ratio of U-235/U-238 and is intended to exclude the transmutation of U-235 to U-236 in the burnup analysis. This data can then be used to correlate the U-235 burnup as measured in PIE to the U-235 depletion calculated in Equation (6).

$$U-235\ Burnup = \frac{\left[\frac{U_{235}}{U_{238}}\right]_{BOL} - \left[\frac{U_{235}+U_{236}}{U_{238}+Pu_{total}}\right]_{EOL}}{\left[\frac{U_{235}}{U_{238}}\right]_{BOL}} \tag{7}$$

# 6. CALCULATED RESULTS

## 6.1 Eigenvalue

For the ATR benchmark cases, the calculated eigenvalue, lobe powers, the AFIP-7 beginning of cycle plate powers, end of irradiation U-235 burnup, U-235 depletion, and fission density are described in this report. Figure 3 and Figure 4 present the calculated eigenvalues for the explicit model and benchmark model for Cycles 149B and 150B, respectively. The more detailed explicit model and benchmark model demonstrate approximately -0.6% Δk/k at the Beginning of Cycle (BOC) in each case. The end of cycle increase to −1.0% and -0.8% Δk/k at the end of cycle for the explicit model and benchmark model, resspectivley . A similar trend is shown for Cycle 150B, with the explicit model and benchmark model showing a bias of -0.7% and -0.6% Δk/k at BOC, respectively. The benchmark model shows a bias at end of cycle -0.8% Δk/k, while the explicit model shows an end of cycle bias of -1.1% Δk/k.

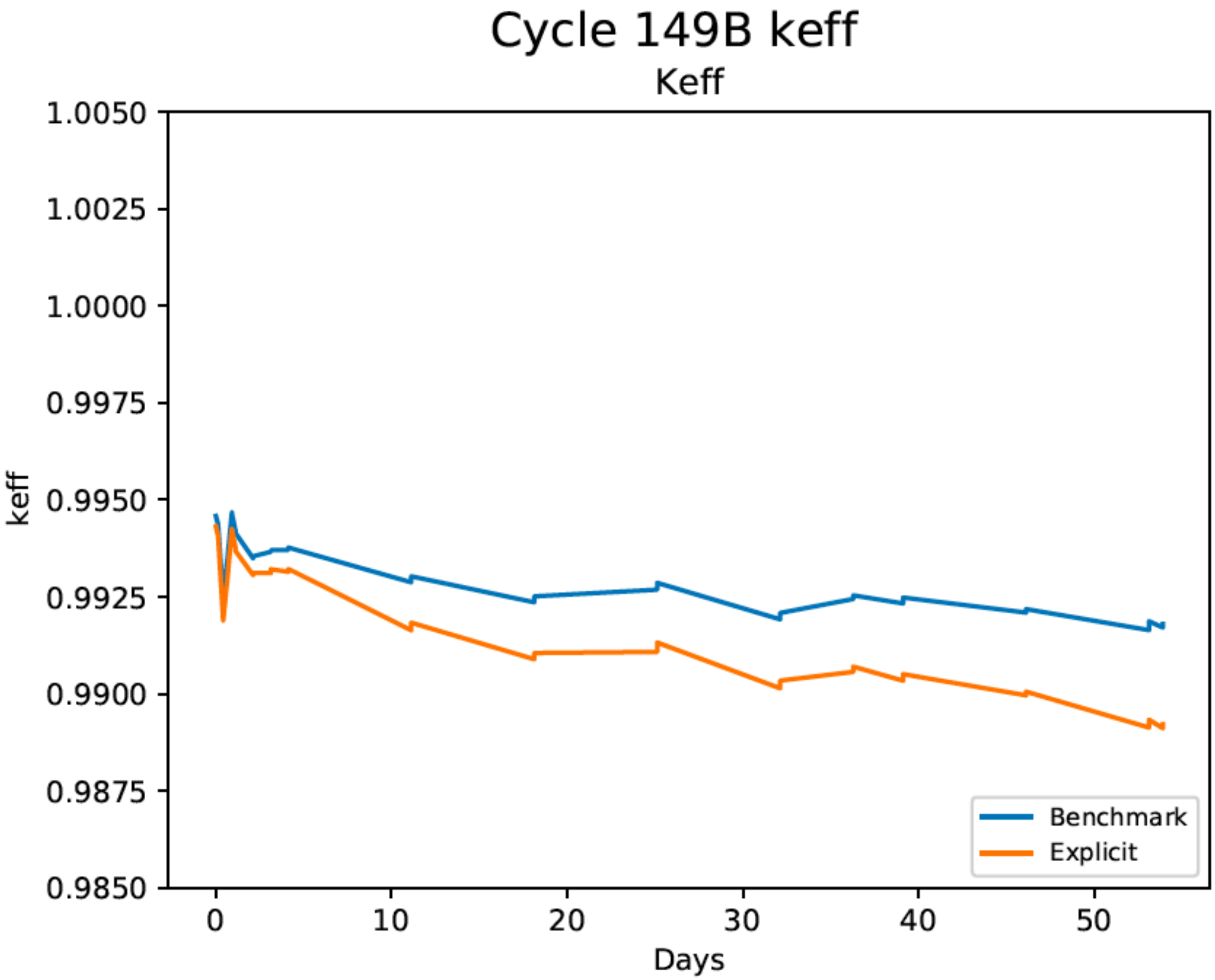

Figure 3. Calculated eigenvalue for Cycle 149B.

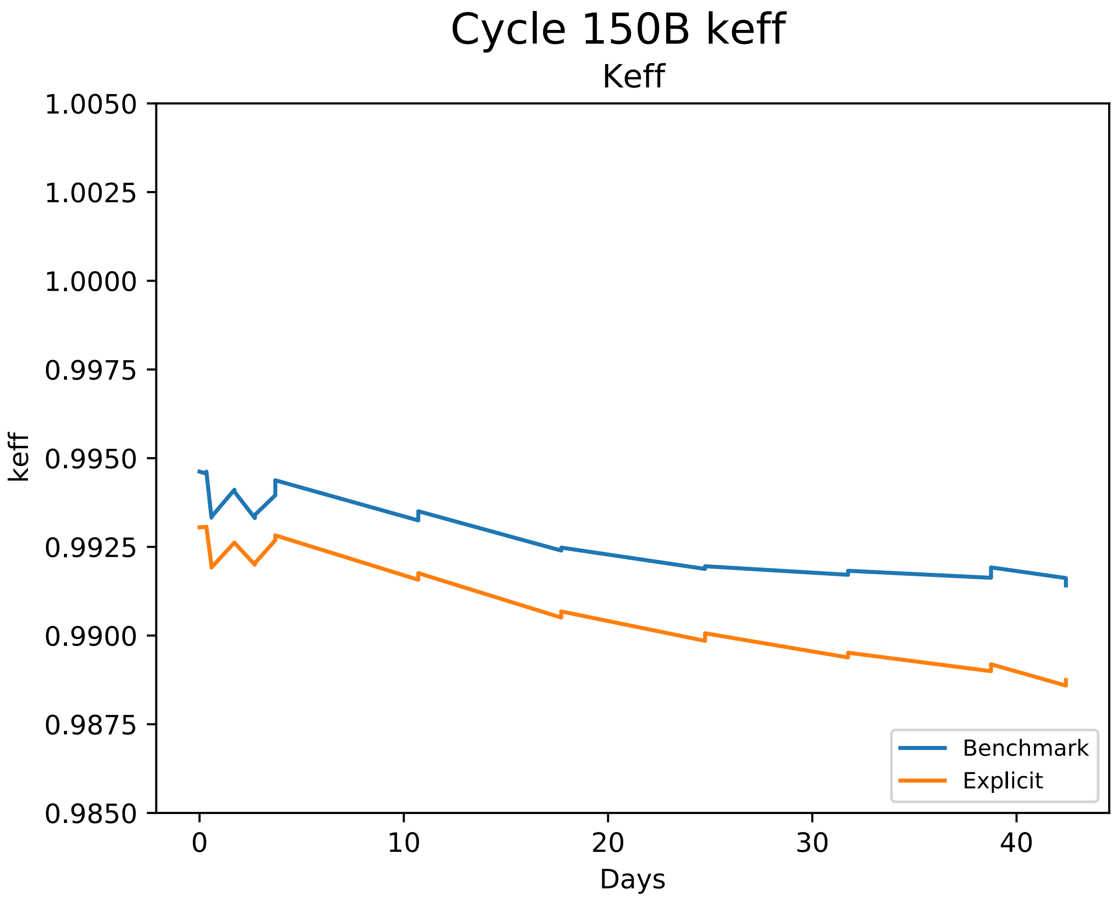

Figure 4. Calculated eigenvalue for Cycle 150B.

## 6.2 Lobe Powers

Figure 5 through Figure 10 provide a comparison of the measured vs. calculated lobe powers from the explicit model and benchmark model for Cycles 149B and 150B. Of primary interest is the center lobe power, which is shown in the center of each figure. Table 14 provides a summary of the integrated lobe source power (MWd) for the center lobe over these two cycles. The total measured source power for the center lobe is 2312 MWd. For the benchmark model, the calculated source power is 2111 MWd (8.7% low), and for the explicit model, the calculated source power is 2153 MWd (6.9% low). The calculated center lobe power demonstrates a consistent bias in the center lobe vs. the measured values. The uncertainty in the lobe power monitoring system is assumed to be 8.5% (2σ). The bias is consistent between the two models and slightly more in the benchmark model. It is anticipated for the benchmark configuration, the bias would be slightly more as the experiment configuration is not modeled with the same configuration as the explicit model, which is a better representation of the reality of the reactor.

The lobe power monitoring system consists of 10 water tubes with one tube in each of the corner lobes, two in the center, and one tube in each of the north, south, east, and west. The activation of oxygen in the tubes is measured and related to the fission power from each of the lobes. The lobe power is determined by solving a system of equations. The matrix of the system on the left-hand side is a 5x11 matrix, where the first 10 rows are related to each of the tubes. The eleventh row is a weighted coefficient to force the solution of the five lobes to be constrained to total core power. The coefficients in each row represent the contribution of fission neutrons from each lobe that results in activation in that particular tube. It should be noted the coefficients used to solve the system of equations have not been updated in the last few decades. Rather, correction factors have been applied as needed to the right-hand side of the system of equations to account for core changes. These factors have been applied to ensure a comparison of the four-quadrant powers measured using the N-16 system and the waterpower calculator agree. Since the center flux trap is split between the four quadrants, it is theorized any bias in the center flux trap would not be easily detected and thus contributes to differences between calculated and measured values. In other words, the physics models may capture reality more accurately than the measurements.

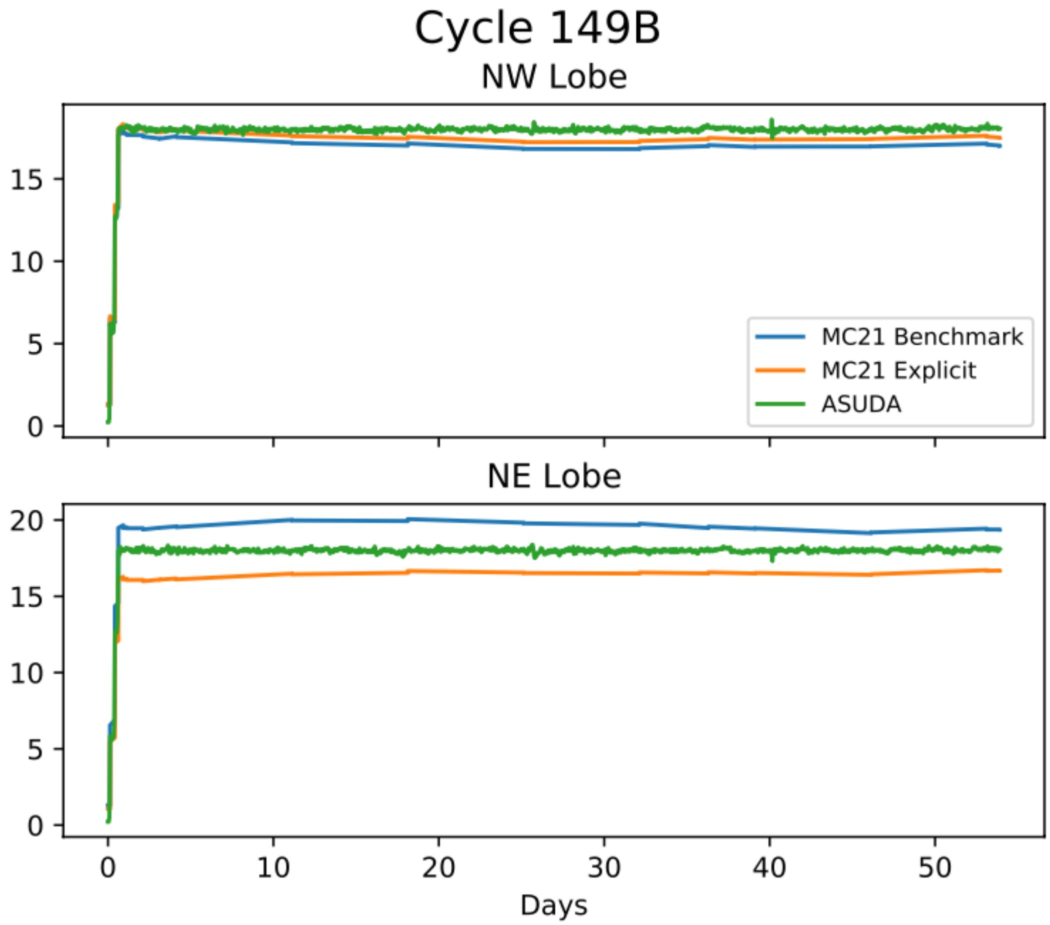

Figure 5. Calculated and measured (ASUDA) NE and NW lobe powers (MW) for the benchmark model and explicit model.

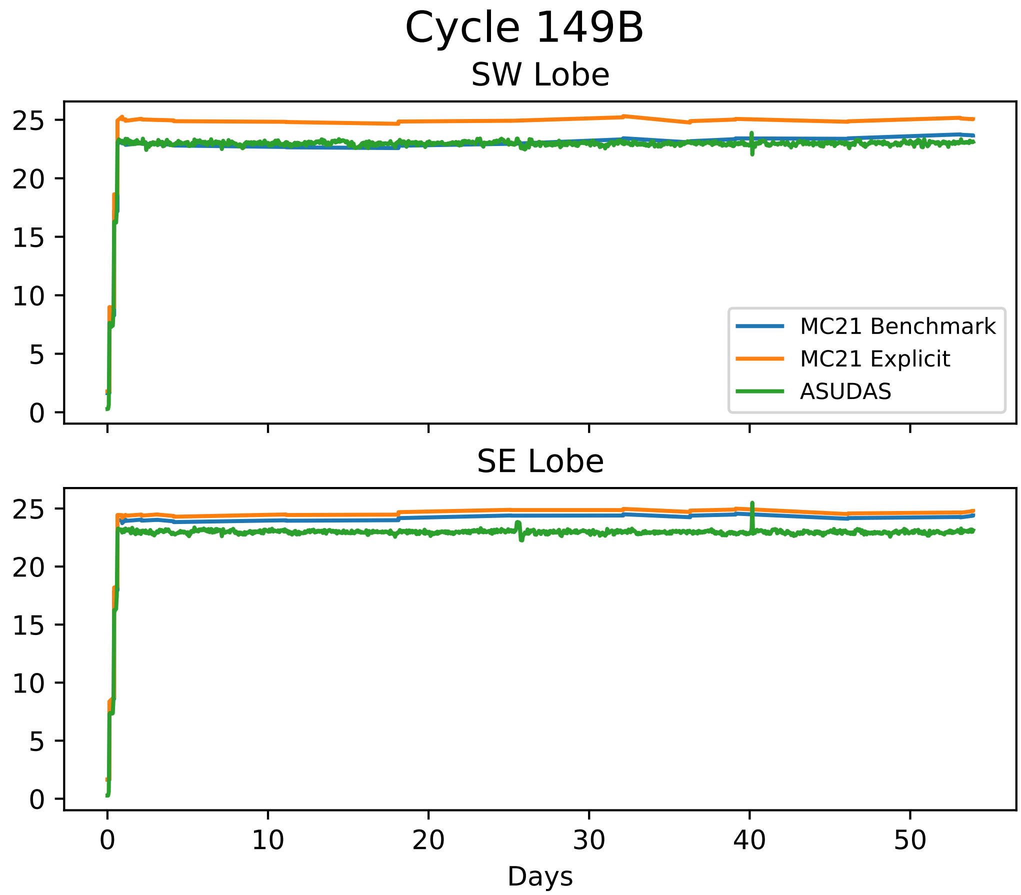

Figure 6. Calculated and measured (ASUDA) SE and SW lobe powers (MW) for the benchmark model and explicit model.

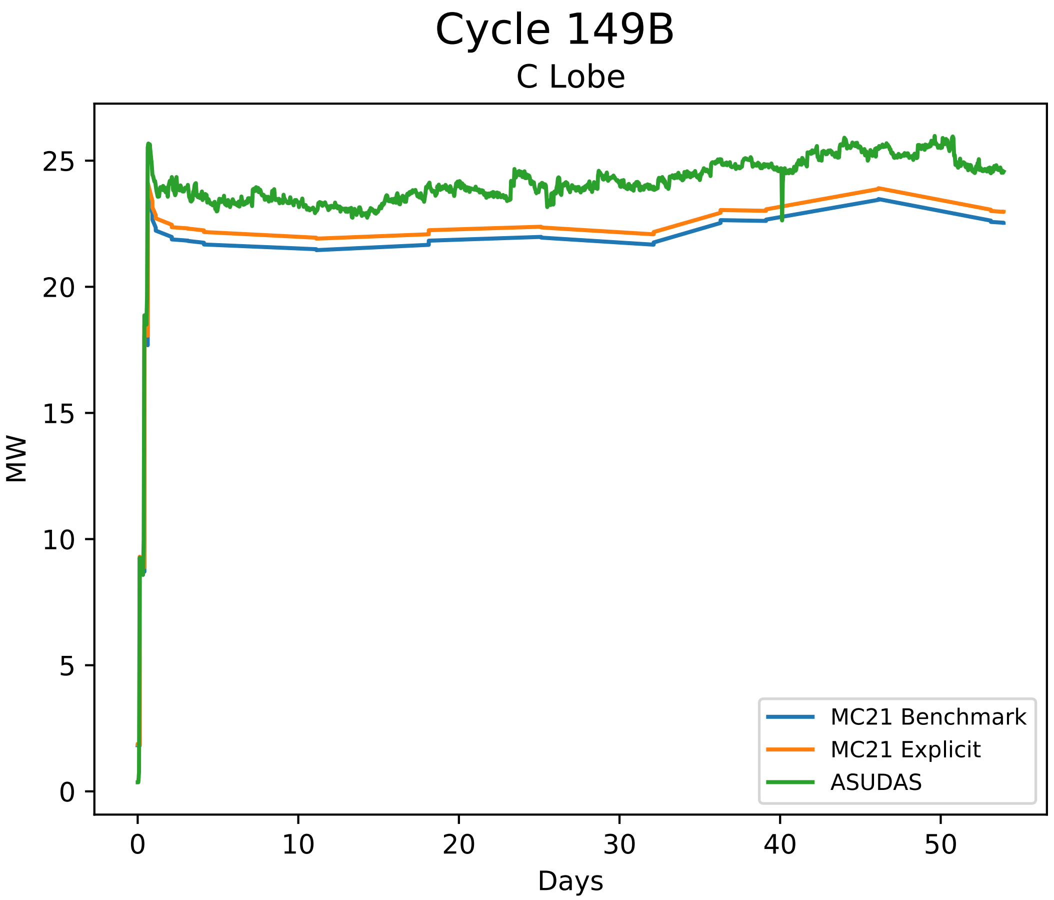

Figure 7. Calculated and measured (ASUDA) C lobe power (MW) for the benchmark model and explicit model.

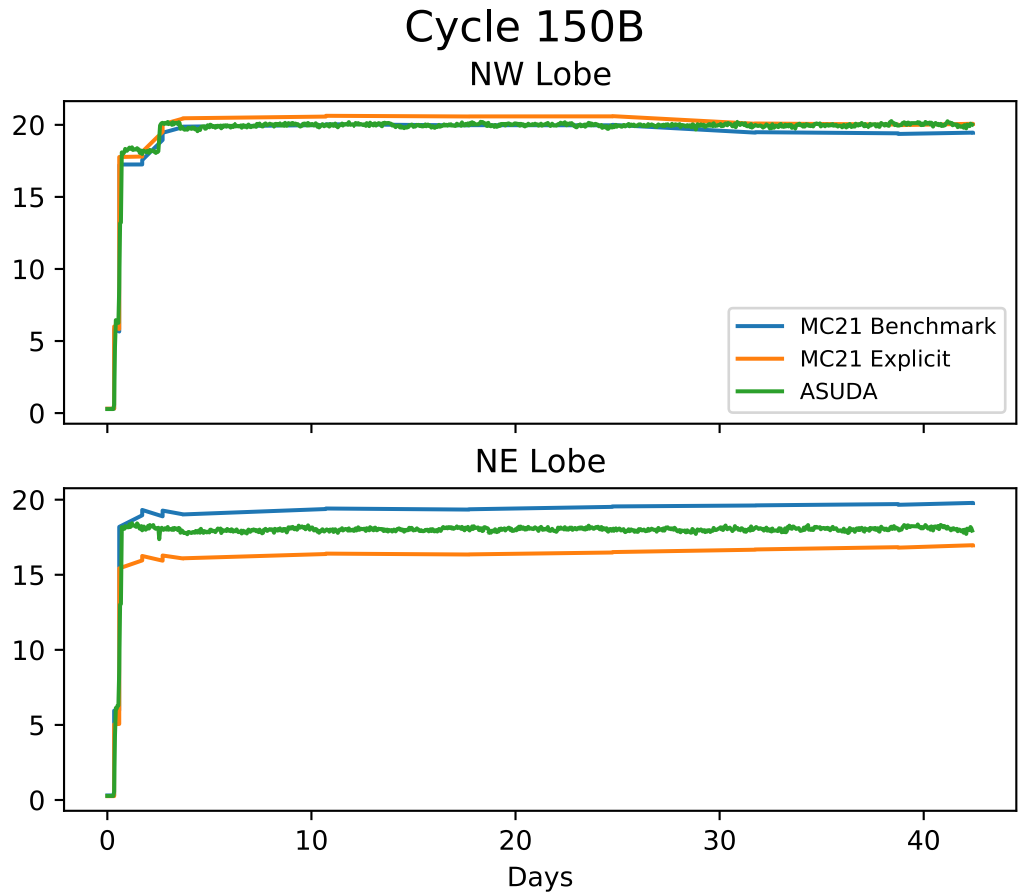

Figure 8. Calculated and measured (ASUDA) NE and NW lobe powers (MW) for the benchmark model and explicit model.

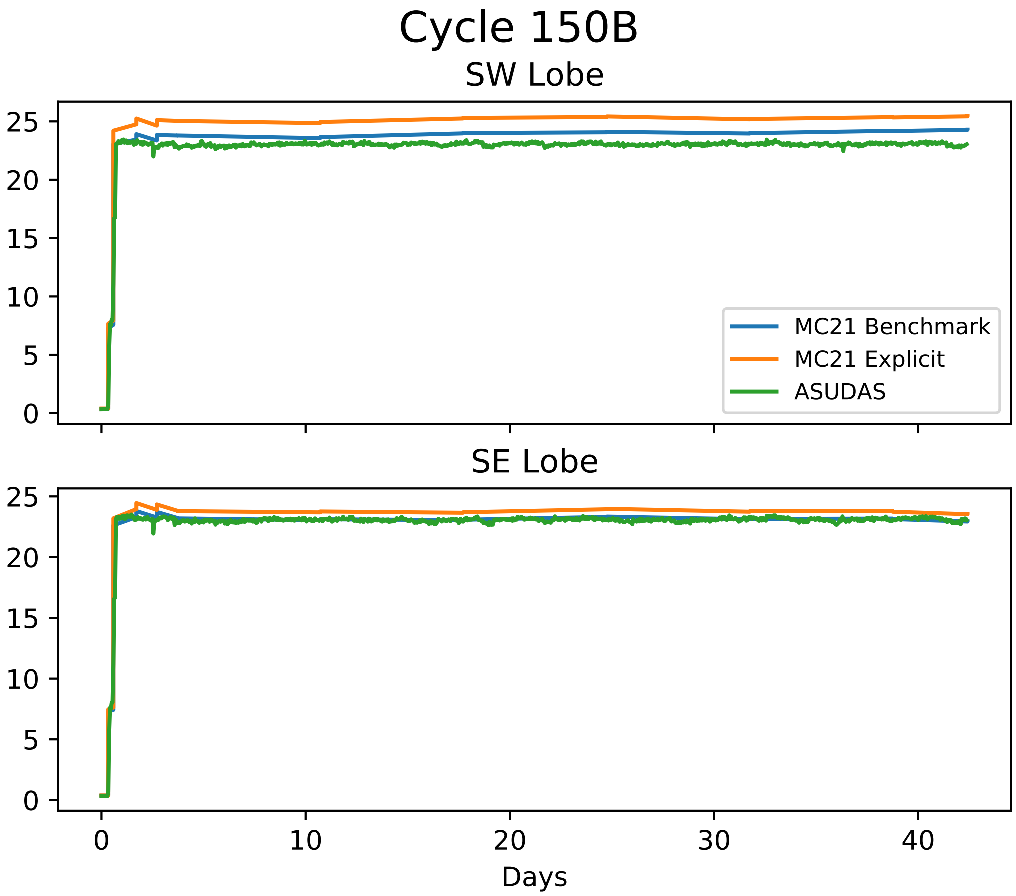

Figure 9. Calculated and measured (ASUDA) SE and SW lobe powers (MW) for the benchmark model and explicit model.

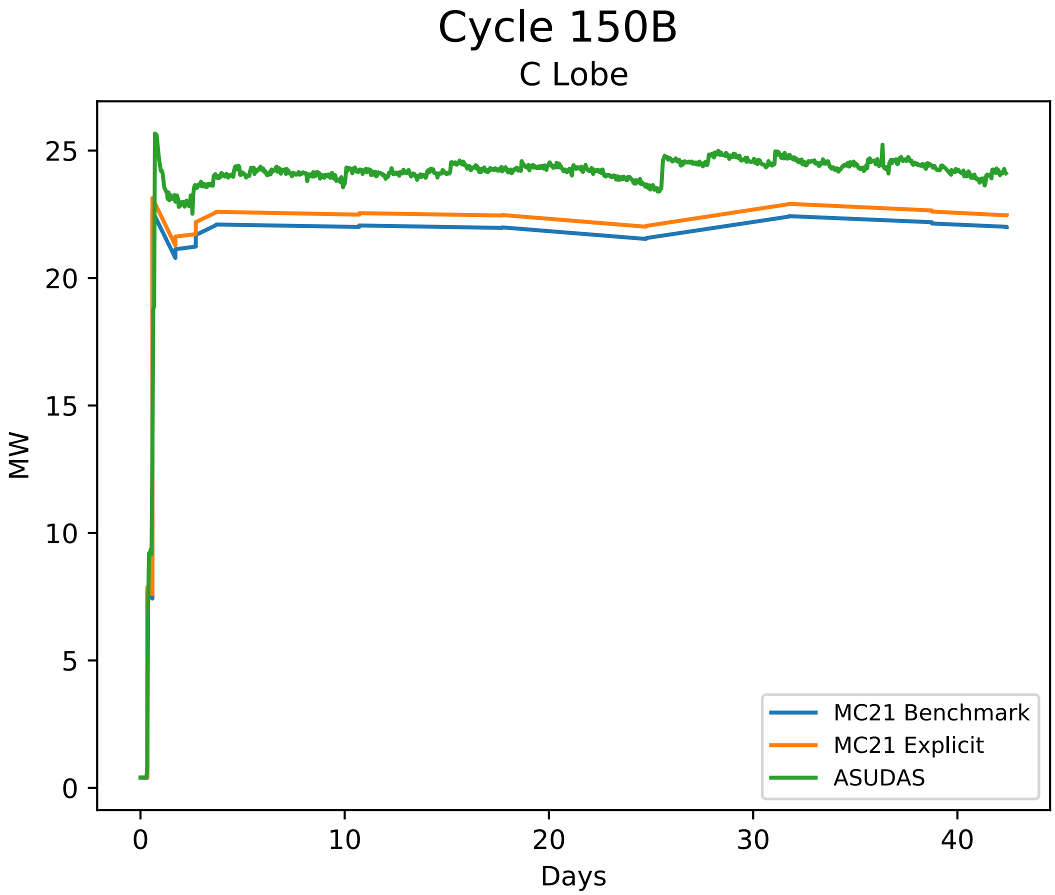

Figure 10. Calculated and measured (ASUDA) C lobe power (MW) for the benchmark model and explicit model.

Table 14. Integrated source powers (MWd) for the center lobe.

| Model | Calculated MWd (Center) | % Difference |
|---|---|---|
| Measured | 2312 | |
| Benchmark Model | 2111 | -8.7% |
| Explicit Model | 2153 | -6.9% |

## 6.3 BOC Experiment Powers

Each AFIP-7 plate was modeled with 10 azimuthal regions and 77 axial regions to provide a high-fidelity model of the depletion. Initial power densities were calculated using the MC21 tally for direct sensible fission energy release. Figure 11 shows the initial power densities when the ATR reached full power for cycle 149B. An interesting note is the peaking that occurs on the edge of the plates above and below core midplane. The peaking is the result of the increased moderation from the holder cutouts. These holder cutouts were used to provide cooling in the unlikely event of a canal handing accident following irradiation. With the exception of the cutouts, the power distribution at the beginning of irradiation is expected with increased fission rate on the edges and near the mid-plane and lower fission rates at the axial edges.

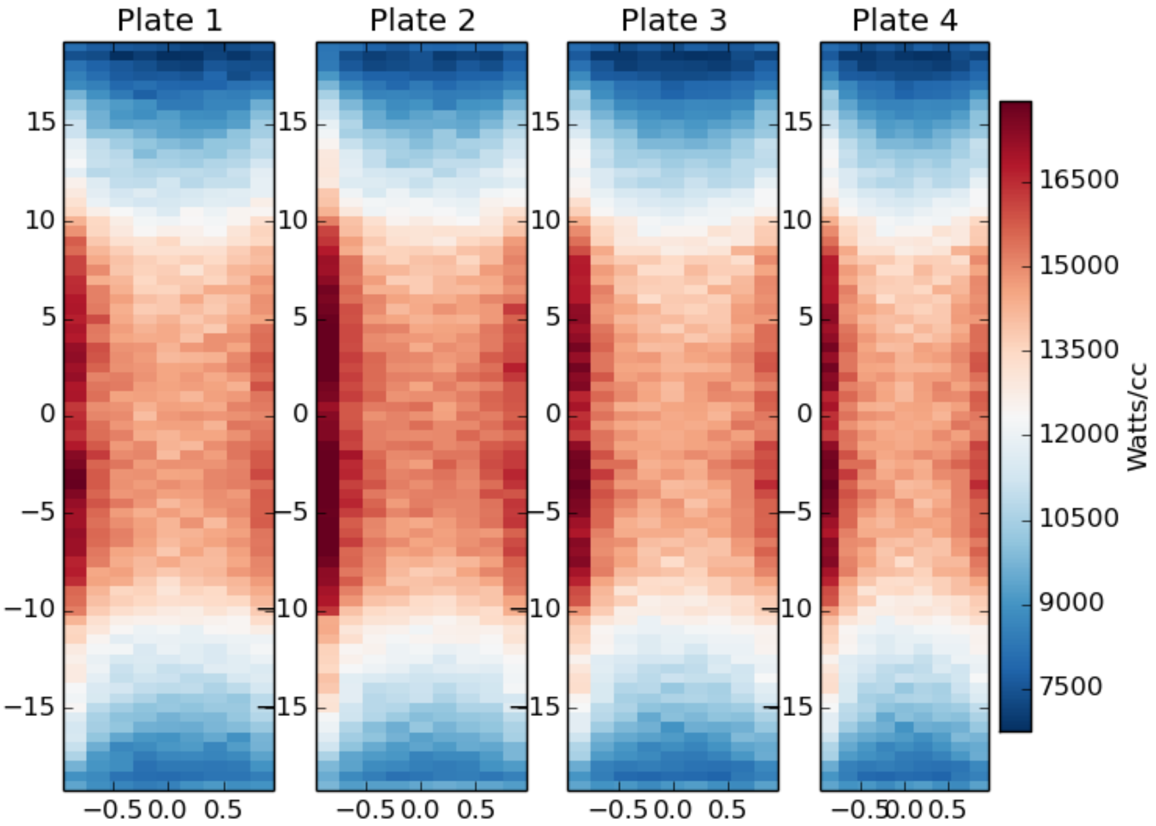

Figure 11. Beginning of life power densities of the AFIP-7 fuel plates.

## 6.4 AFIP-7 Burnup Values

The AFIP-7 U-235 burnup results for the benchmark and explicit model are presented in Figure 12 and Figure 13, respectively. The U-235 burnup formula is presented in Section 5.4. The U-235 burnup is measured based on the ratio of U-235 to total U and Pu. In comparing the two cases, the U-235 burnup is approximately 40% to 43% on the edge of the plates above and below the mid-plane of the plate as the result of the coolant vents. It should be noted the two cases visually provide identical results. A summary of the U-235 burnup values is presented in Table 15. The burnup values are 20% higher at the top of the plate compared to 10% lower at the bottom of the plate. However, the burnup near core mid-plane is well within the uncertainty of the calculated powers, given the uncertainty in the center lobe power is 8.5%. The discrepancy at the top and bottom may be related to the gradient seen in the burnup of the plates at the axial locations. Discussions with the PIE principal investigators indicated the exact location of the fuel relative to core centerline cannot be accurately determined, which may have resulted in slight discrepancies between the measured and calculated results on the edge of the plates.

Similar to the U-235 burnup calculation, the depletion results are provided in Figure 14 and Figure 15. Since the exact mass of U-235 cannot be determined from chemistry samples, it is not possible to compare measured to calculated values. The results are presented in this report for information. As seen in the burnup results, the depletion values are nearly identical.

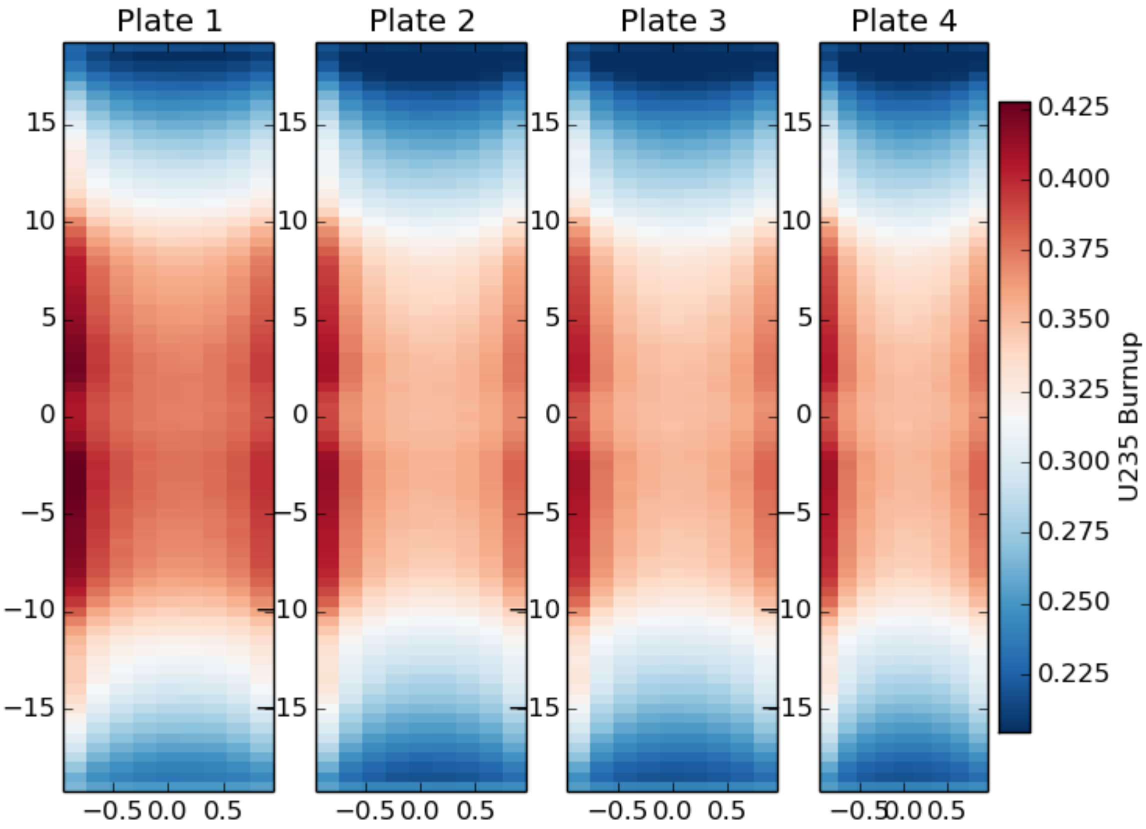

Figure 12. U-235 burnup for the AFIP-7 plates using the benchmark model.

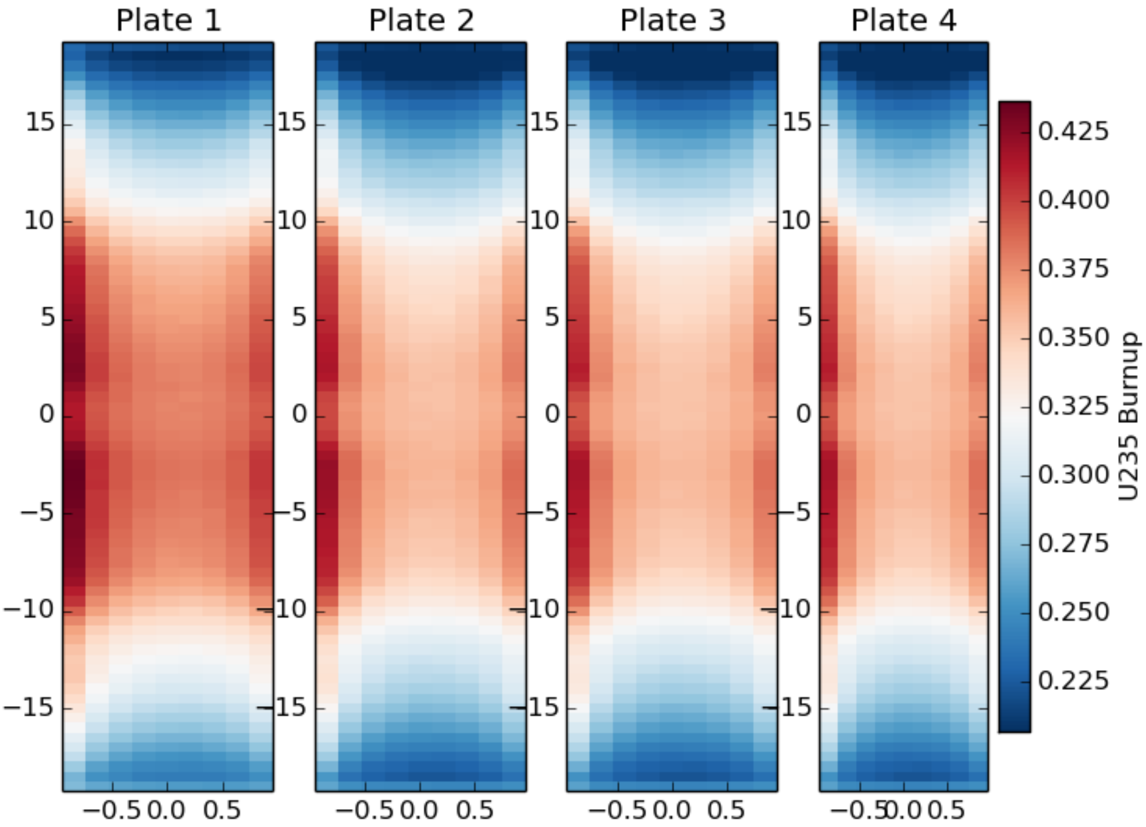

Figure 13. U-235 burnup for the AFIP-7 plates using the explicit model.

Table 15. Calculated vs. measured U-235 burnup for AFIP-7 Plate 2.

| Sample | Location | Distance from Core Midplane (in.) | Measured Burnup | MC21 Calculated Burnup (Benchmark Model) | MC21 Calculated Burnup (Explicit Model) | Benchmark Model C/M | Explicit Model C/M |
|---|---|---|---|---|---|---|---|
| 1664 | Cross section top of foil | 18.25 | 17.18% | 20.39% | 20.59% | 1.19 | 1.20 |
| 2274 | Cross section top of foil | 16.25 | 21.16% | 24.38% | 24.65% | 1.15 | 1.16 |
| 2275 | Cross section at centerline | 1.75 | 36.54% | 36.38% | 36.99% | 1.00 | 1.01 |
| 2276 | Left edge at centerline | -0.25 | 41.68% | 39.83% | 40.52% | 0.96 | 0.97 |
| 2277 | Left center at center line | -0.25 | 35.66% | 35.88% | 36.53% | 1.01 | 1.02 |
| 2278 | Right center at centerline | -0.25 | 34.89% | 36.05% | 36.52% | 1.03 | 1.05 |
| 2279 | Right edge at center line | -0.25 | 40.09% | 39.97% | 40.43% | 1.00 | 1.01 |
| 2280 | Left edge at bottom of foil | -17.25 | 32.15% | 27.33% | 28.05% | 0.85 | 0.87 |
| 2281 | Left center at bottom of foil | -17.25 | 26.02% | 22.97% | 23.55% | 0.88 | 0.91 |
| 2282 | Right center at bottom of foil | -17.25 | 27.05% | 23.83% | 24.10% | 0.88 | 0.89 |
| 2284 | Right edge at bottom of foil | -17.25 | 30.73% | 27.38% | 27.93% | 0.89 | 0.91 |
| 2285 | Cross section at bottom of foil | -17.73 | 26.72% | 23.55% | 24.05% | 0.88 | 0.90 |

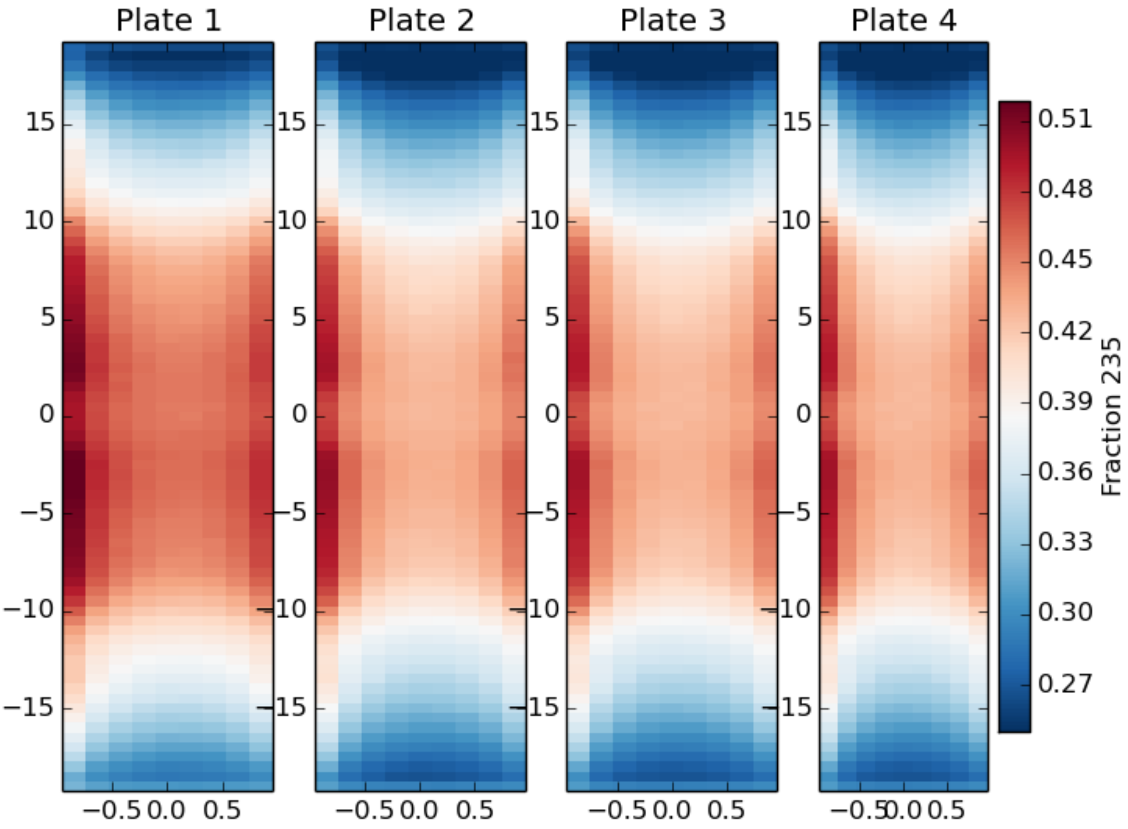

Figure 14. Calculated U-235 depletion for the AFIP-7 experiments in the benchmark model.

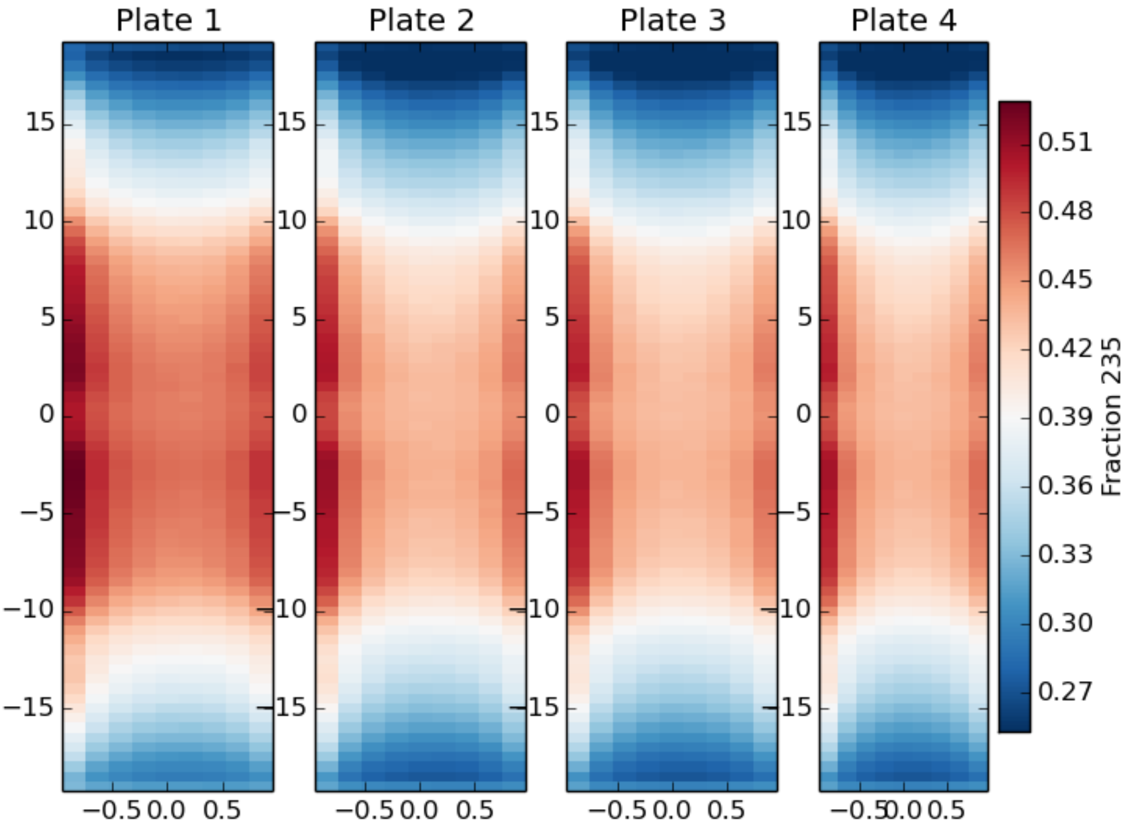

Figure 15. Calculated U-235 depletion for the AFIP-7 experiments in the explicit model.

Of importance to the benchmark model is the calculated fission density compared to the measured fission density. Several methods have been employed to determine actual fission density from measured values. One particular method is to use fission product isotopes that have similar fission product yields for U-235 and Pu-239. This allows one to estimate the number of fissions based on the number of fission products present. Chemical destructive analysis was performed on Plates 2 and 4. The measured fission product nuclides for Plates 2 and Plates 4 are presented in Table 16 and Table 19, respectively. The measured actinide content of the samples is presented in Table 17 and Table 20. The data above can be used to calculate the total number of initial heavy metal atoms in a sample. Assuming the as-built actinide density, the fission density can be determined. The fission density for Plates 2 and 4 are presented in

Table 19 and Table 21, respectively. The fission density for Plate 2 is consistent with the calculated to measured values for U-235 burnup presented above. The fission density values are approximately 10% high near the top of the plate, in good agreement near plate centerline, and 10% low at the bottom of the plate.

The fission density for Plate 4 shows a much larger bias. The bias at the top and middle of the plate is approximately 20% and 10%, while there is no bias at the bottom. It is not clear why the differences at this point exist and may require additional evaluation.

Additional comparisons can be made relative to the PIE data. Gamma scans were performed for each of the four plates. Figure 18 through Figure 21 a comparison between the normalized gamma scan data and the calculated local-to-average (L2AR) fission density values. As can be seen, the data appears to be consistently shifted when compared to the gamma scan data. This trend is consistent among the four plates as well a destructive PIE data on Plates 2 and 4. Given the results presented in this report, it appears that an axial bias exists in the model and is consistent in all four plates. However, the discrepancy noted on Plate 4 warrants further investigation.

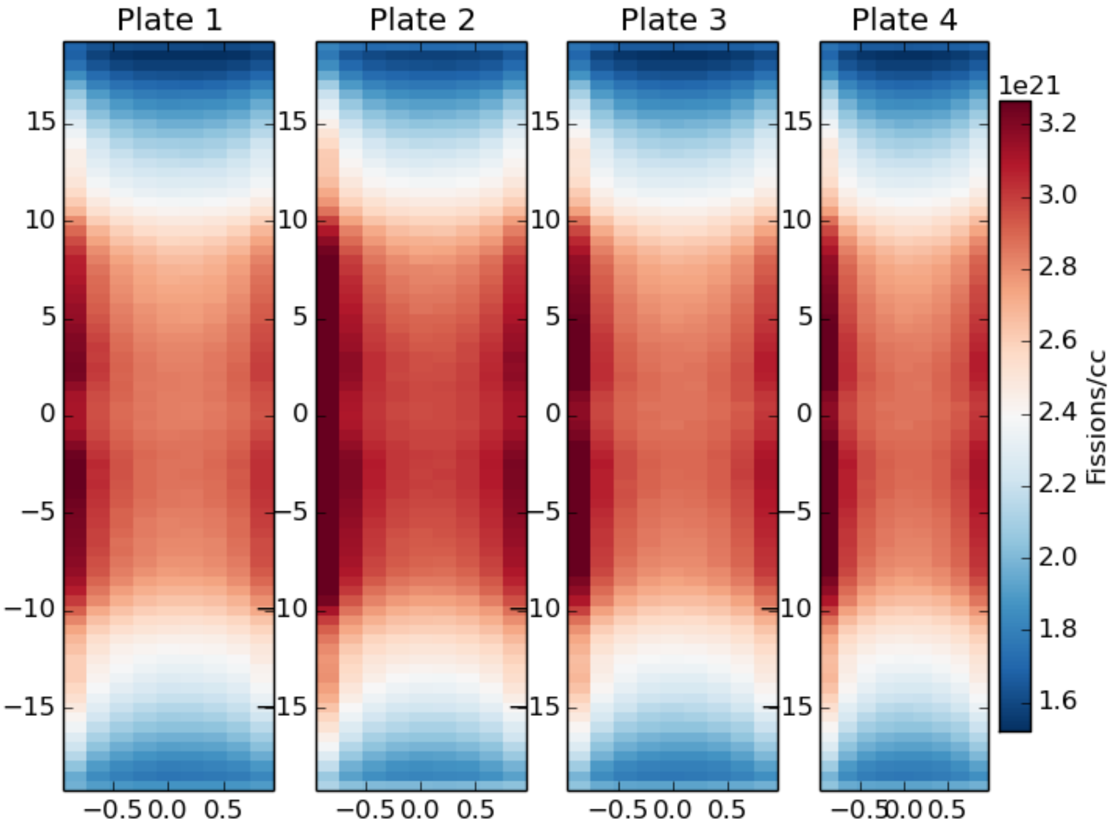

Figure 16. Fission density for the AFIP-7 plates in the benchmark model.

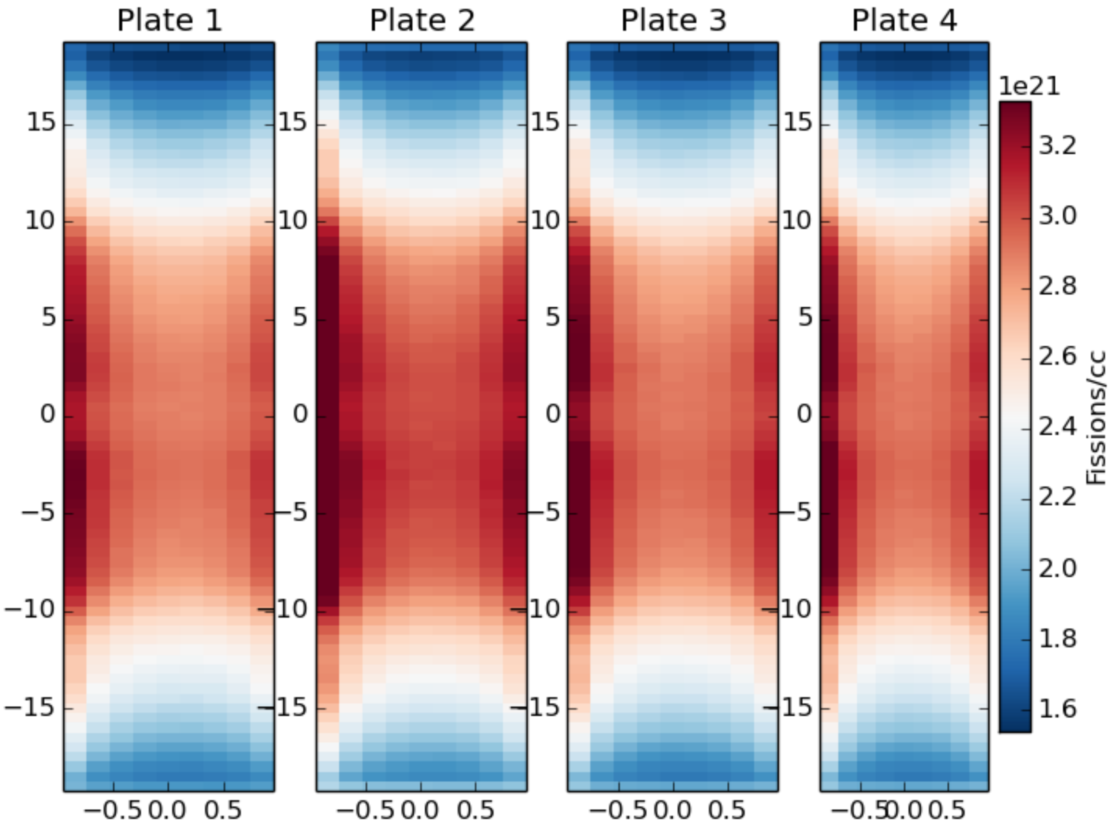

Figure 17. Fission density for the AFIP-7 plates in the explicit model.

Table 16. Measured fission product nuclides from each sample in Plate 2 (atoms/cm$^3$).

| Sample | Location | Distance from Core Midplane (in.) | 139La | 140Ce | 141Pr | 143Nd | 144Nd | 143/144Nd | 145Nd | 146Nd | 145/146Nd |
|---|---|---|---|---|---|---|---|---|---|---|---|
| Fission Product Yield (%) | | | 6.41 | 6.22 | 5.85 | 5.96 | 5.50 | 11.46 | 3.93 | 3.00 | 6.93 |
| KGT 1664 | Cross section top of foil | 18.25 | 3.48E+18 | 3.28E+18 | 3.07E+18 | 5.06E+19 | 5.49E+19 | 1.05E+20 | 5.09E+19 | 5.34E+19 | 1.04E+20 |
| KGT 2274 | Cross section top of foil | 16.25 | 4.16E+18 | 3.90E+18 | 3.68E+18 | 6.05E+19 | 6.70E+19 | 1.27E+20 | 6.13E+19 | 6.48E+19 | 1.26E+20 |
| KGT 2275 | Cross section at centerline | 1.75 | 7.33E+18 | 6.97E+18 | 6.50E+18 | 1.00E+20 | 1.26E+20 | 2.27E+20 | 1.06E+20 | 1.18E+20 | 2.23E+20 |
| KGT 2276 | Left edge at centerline | -0.25 | 5.03E+18 | 4.82E+18 | 4.57E+18 | 7.00E+19 | 8.90E+19 | 1.59E+20 | 7.48E+19 | 8.41E+19 | 1.59E+20 |
| KGT 2277 | Left center at center line | -0.25 | 7.59E+18 | 7.19E+18 | 6.75E+18 | 1.05E+20 | 1.31E+20 | 2.36E+20 | 1.10E+20 | 1.24E+20 | 2.34E+20 |
| KGT 2278 | Right center at centerline | -0.25 | 7.46E+18 | 7.19E+18 | 6.67E+18 | 1.04E+20 | 1.29E+20 | 2.33E+20 | 1.08E+20 | 1.21E+20 | 2.29E+20 |
| KGT 2279 | Right edge at center line | -0.25 | 5.90E+18 | 5.64E+18 | 5.30E+18 | 7.99E+19 | 1.03E+20 | 1.83E+20 | 8.57E+19 | 9.73E+19 | 1.83E+20 |
| KGT 2280 | Left edge at bottom of foil | -17.25 | 4.13E+18 | 4.00E+18 | 3.70E+18 | 5.88E+19 | 7.06E+19 | 1.29E+20 | 6.07E+19 | 6.71E+19 | 1.28E+20 |
| KGT 2281 | Left center at bottom of foil | -17.25 | 5.55E+18 | 5.30E+18 | 4.92E+18 | 7.99E+19 | 9.21E+19 | 1.72E+20 | 8.25E+19 | 8.78E+19 | 1.70E+20 |
| KGT 2282 | Right center at bottom of foil | -17.25 | 5.16E+18 | 4.86E+18 | 4.57E+18 | 7.42E+19 | 8.60E+19 | 1.60E+20 | 7.68E+19 | 8.30E+19 | 1.60E+20 |
| KGT 2284 | Right edge at bottom of foil | -17.25 | 4.05E+18 | 3.87E+18 | 3.64E+18 | 5.71E+19 | 6.89E+19 | 1.26E+20 | 5.94E+19 | 6.41E+19 | 1.24E+20 |
| KGT 2285 | Cross section at bottom of foil | -17.73 | 5.29E+18 | 5.04E+18 | 4.70E+18 | 7.64E+19 | 8.83E+19 | 1.65E+20 | 7.82E+19 | 8.45E+19 | 1.63E+20 |

Table 17. Measured actinides from Plate 2.

| 234U | 235U | 236U | 238U | 239Pu | 240Pu | 241M/z | 242Pu | Total HM |
|---|---|---|---|---|---|---|---|---|
| atoms | atoms | atoms | atoms | atoms | atoms | atoms | atoms | atoms |
| 2.62E+18 | 2.17E+20 | 1.16E+19 | 1.10E+21 | 4.66E+18 | 4.01E+17 | 1.08E+17 | 5.10E+15 | 1.33E+21 |
| 2.78E+18 | 2.09E+20 | 1.40E+19 | 1.12E+21 | 5.52E+18 | 5.67E+17 | 1.92E+17 | 1.07E+16 | 1.36E+21 |
| 2.48E+18 | 1.56E+20 | 2.29E+19 | 1.11E+21 | 7.79E+18 | 1.35E+18 | 7.20E+17 | 8.96E+16 | 1.30E+21 |
| 1.42E+18 | 9.66E+19 | 1.58E+19 | 7.62E+20 | 5.47E+18 | 1.01E+18 | 5.32E+17 | 7.54E+16 | 8.82E+20 |
| 2.37E+18 | 1.65E+20 | 2.28E+19 | 1.15E+21 | 8.36E+18 | 1.43E+18 | 7.50E+17 | 9.33E+16 | 1.35E+21 |
| 2.43E+18 | 1.64E+20 | 2.34E+19 | 1.14E+21 | 8.31E+18 | 1.42E+18 | 7.60E+17 | 9.36E+16 | 1.34E+21 |
| 1.98E+18 | 1.13E+20 | 1.91E+19 | 8.73E+20 | 6.63E+18 | 1.24E+18 | 6.70E+17 | 9.73E+16 | 1.02E+21 |
| 1.76E+18 | 1.14E+20 | 1.29E+19 | 7.39E+20 | 4.96E+18 | 7.35E+17 | 3.05E+17 | 3.06E+16 | 8.73E+20 |
| 2.78E+18 | 1.99E+20 | 1.76E+19 | 1.16E+21 | 7.05E+18 | 9.16E+17 | 3.85E+17 | 2.94E+16 | 1.39E+21 |
| 2.52E+18 | 1.83E+20 | 1.65E+19 | 1.09E+21 | 6.55E+18 | 8.43E+17 | 3.52E+17 | 2.91E+16 | 1.30E+21 |
| 1.85E+18 | 1.20E+20 | 1.33E+19 | 7.64E+20 | 4.84E+18 | 7.10E+17 | 3.07E+17 | 2.81E+16 | 9.06E+20 |
| 2.70E+18 | 1.97E+20 | 1.80E+19 | 1.16E+21 | 6.73E+18 | 8.73E+17 | 3.57E+17 | 2.86E+16 | 1.39E+21 |

Table 18. Measured and Calculated Fission Density (fission/$cm^3$) for Plate 2 from the Benchmark Model.

| Sample | Location | Distance from Core Midplane (in.) | 139La | 140Ce | 141Pr | 145/146Nd | 143/144Nd | Average | Calculated | C/M |
|---|---|---|---|---|---|---|---|---|---|---|
| KGT 1664 | Cross section top of foil | 18.25 | 1.57E+21 | 1.52E+21 | 1.52E+21 | 1.50E+21 | 1.52E+21 | 1.53E+21 | 1.69E+21 | 1.11 |
| KGT 2274 | Cross section top of foil | 16.25 | 1.83E+21 | 1.77E+21 | 1.77E+21 | 1.77E+21 | 1.79E+21 | 1.79E+21 | 2.03E+21 | 1.14 |
| KGT 2275 | Cross section at centerline | 1.75 | 3.23E+21 | 3.17E+21 | 3.14E+21 | 3.14E+21 | 3.19E+21 | 3.17E+21 | 3.08E+21 | 0.97 |
| KGT 2276 | Left edge at centerline | -0.25 | 3.27E+21 | 3.23E+21 | 3.26E+21 | 3.28E+21 | 3.29E+21 | 3.27E+21 | 3.38E+21 | 1.03 |
| KGT 2277 | Left center at center line | -0.25 | 3.22E+21 | 3.15E+21 | 3.14E+21 | 3.16E+21 | 3.20E+21 | 3.17E+21 | 3.04E+21 | 0.96 |
| KGT 2278 | Right center at centerline | -0.25 | 3.20E+21 | 3.18E+21 | 3.14E+21 | 3.13E+21 | 3.19E+21 | 3.17E+21 | 3.05E+21 | 0.96 |
| KGT 2279 | Right edge at center line | -0.25 | 3.32E+21 | 3.28E+21 | 3.28E+21 | 3.28E+21 | 3.30E+21 | 3.29E+21 | 3.39E+21 | 1.03 |
| KGT 2280 | Left edge at bottom of foil | -17.25 | 2.75E+21 | 2.75E+21 | 2.70E+21 | 2.71E+21 | 2.75E+21 | 2.73E+21 | 2.28E+21 | 0.83 |
| KGT 2281 | Left center at bottom of foil | -17.25 | 2.35E+21 | 2.31E+21 | 2.28E+21 | 2.30E+21 | 2.33E+21 | 2.31E+21 | 1.91E+21 | 0.83 |
| KGT 2282 | Right center at bottom of foil | -17.25 | 2.34E+21 | 2.28E+21 | 2.28E+21 | 2.31E+21 | 2.32E+21 | 2.31E+21 | 1.99E+21 | 0.86 |
| KGT 2284 | Right edge at bottom of foil | -17.25 | 2.61E+21 | 2.58E+21 | 2.57E+21 | 2.54E+21 | 2.60E+21 | 2.58E+21 | 2.28E+21 | 0.88 |
| KGT 2285 | Cross section at bottom of foil | -17.73 | 2.24E+21 | 2.20E+21 | 2.19E+21 | 2.20E+21 | 2.23E+21 | 2.21E+21 | 1.96E+21 | 0.89 |

Table 19. Measured fission product nuclides for Plate 4 (atoms/cm$^3$).

| Sample | Location | Distance from Core Midplane (in.) | 139La | 141Pr | 143Nd | 144Nd | 143/144Nd | 145Nd | 146Nd | 145/146Nd |
|---|---|---|---|---|---|---|---|---|---|---|
| Fission Product Yield (%) | | | 6.41 | 5.85 | 5.96 | 5.50 | 11.46 | 3.93 | 9.43 | 13.36 |
| KGT 2488 | Cross section top of foil | 18.25 | 1.94E+20 | 1.93E+20 | 1.85E+20 | 2.04E+20 | 3.89E+20 | 1.89E+20 | 1.98E+20 | 3.87E+20 |
| KGT 2513 | Cross section top of foil | 16.25 | 2.04E+20 | 2.01E+20 | 1.91E+20 | 2.15E+20 | 4.06E+20 | 1.96E+20 | 2.06E+20 | 4.02E+20 |
| KGT 2526 | Cross section at centerline | 1.75 | 3.98E+20 | 3.81E+20 | 3.39E+20 | 4.36E+20 | 7.75E+20 | 3.62E+20 | 4.09E+20 | 7.70E+20 |
| KGT 2538 | Left edge at centerline | -0.25 | 2.31E+19 | 2.28E+19 | 1.99E+19 | 2.63E+19 | 4.62E+19 | 2.15E+19 | 2.44E+19 | 4.58E+19 |
| KGT 2550 | Left center at center line | -0.25 | 1.39E+20 | 1.38E+20 | 1.23E+20 | 1.56E+20 | 2.79E+20 | 1.30E+20 | 1.46E+20 | 2.76E+20 |
| KGT 1981 | Right center at centerline | -0.25 | 1.49E+20 | 1.47E+20 | 1.32E+20 | 1.67E+20 | 3.00E+20 | 1.40E+20 | 1.58E+20 | 2.98E+20 |
| KGT 1975 | Right edge at center line | -0.25 | 1.14E+19 | 1.13E+19 | 9.97E+18 | 1.30E+19 | 2.30E+19 | 1.07E+19 | 1.21E+19 | 2.28E+19 |
| KGT 1978 | Left edge at bottom of foil | -17.25 | 1.41E+19 | 1.40E+19 | 1.29E+19 | 1.56E+19 | 2.85E+19 | 1.34E+19 | 1.47E+19 | 2.82E+19 |
| KGT 1965 | Left center at bottom of foil | -17.25 | 1.24E+20 | 1.22E+20 | 1.14E+20 | 1.33E+20 | 2.47E+20 | 1.17E+20 | 1.27E+20 | 2.44E+20 |
| KGT 1968 | Right center at bottom of foil | -17.25 | 1.00E+20 | 9.86E+19 | 9.26E+19 | 1.08E+20 | 2.01E+20 | 9.57E+19 | 1.03E+20 | 1.99E+20 |
| KGT 1972 | Right edge at bottom of foil | -17.25 | 1.48E+19 | 1.45E+19 | 1.34E+19 | 1.61E+19 | 2.95E+19 | 1.40E+19 | 1.51E+19 | 2.91E+19 |
| KGT 1971 | Cross section at bottom of foil | -17.73 | 2.71E+20 | 2.59E+20 | 2.40E+20 | 2.82E+20 | 5.22E+20 | 2.49E+20 | 2.63E+20 | 5.11E+20 |

Table 20. Measured actinides for Plate 4.

| 234U | 235U | 236U | 238U | 239Pu | 240Pu | 241M/z | Total HM |
|---|---|---|---|---|---|---|---|
| atoms | atoms | atoms | atoms | atoms | atoms | atoms | atoms |
| 9.26E+18 | 7.25E+20 | 4.06E+19 | 3.69E+21 | 1.70E+19 | 1.54E+18 | 4.72E+17 | 4.49E+21 |
| 8.96E+18 | 6.59E+20 | 4.62E+19 | 3.54E+21 | 2.23E+19 | 2.35E+18 | 7.77E+17 | 4.28E+21 |
| 8.65E+18 | 5.10E+20 | 7.81E+19 | 3.72E+21 | 2.72E+19 | 4.82E+18 | 2.47E+18 | 4.35E+21 |
| 4.76E+17 | 2.77E+19 | 4.80E+18 | 2.14E+20 | 1.79E+18 | 3.34E+17 | 1.76E+17 | 2.49E+20 |
| 3.27E+18 | 1.91E+20 | 2.88E+19 | 1.39E+21 | 1.16E+19 | 2.03E+18 | 1.06E+18 | 1.63E+21 |
| 3.47E+18 | 2.09E+20 | 3.09E+19 | 1.51E+21 | 1.27E+19 | 2.21E+18 | 1.16E+18 | 1.77E+21 |
| 2.36E+17 | 1.33E+19 | 2.26E+18 | 1.01E+20 | 8.87E+17 | 1.66E+17 | 8.79E+16 | 1.18E+20 |
| 4.25E+17 | 2.69E+19 | 2.96E+18 | 1.71E+20 | 1.22E+18 | 1.77E+17 | 7.30E+16 | 2.03E+20 |
| 3.86E+18 | 2.87E+20 | 2.63E+19 | 1.70E+21 | 1.22E+19 | 1.58E+18 | 6.50E+17 | 2.03E+21 |
| 3.27E+18 | 2.38E+20 | 2.21E+19 | 1.40E+21 | 9.78E+18 | 1.27E+18 | 5.22E+17 | 1.67E+21 |
| 4.37E+17 | 2.79E+19 | 3.16E+18 | 1.78E+20 | 1.27E+18 | 1.83E+17 | 7.65E+16 | 2.11E+20 |
| 8.70E+18 | 6.05E+20 | 5.56E+19 | 3.57E+21 | 2.17E+19 | 2.86E+18 | 1.09E+18 | 4.26E+21 |

Table 21. Measured and calculated fission density (fissions/cm$^3$) for Plate 4 from the benchmark model.

| Sample | Location | Distance from Core Midplane (in.) | 139La | 141Pr | 145/146Nd | 143/144Nd | Average | Calculated | C/M |
|---|---|---|---|---|---|---|---|---|---|
| KGT 2488 | Cross section top of foil | 18.25 | 1.50E+21 | 1.49E+21 | 1.49E+21 | 1.50E+21 | 1.49E+21 | 1.76E+21 | 1.18 |
| KGT 2513 | Cross section top of foil | 16.25 | 1.65E+21 | 1.62E+21 | 1.62E+21 | 1.63E+21 | 1.63E+21 | 2.11E+21 | 1.29 |
| KGT 2526 | Cross section at centerline | 1.75 | 3.03E+21 | 2.91E+21 | 2.92E+21 | 2.94E+21 | 2.95E+21 | 3.18E+21 | 1.08 |
| KGT 2538 | Left edge at centerline | -0.25 | 3.07E+21 | 3.03E+21 | 3.02E+21 | 3.05E+21 | 3.05E+21 | 3.37E+21 | 1.11 |
| KGT 2550 | Left center at center line | -0.25 | 2.85E+21 | 2.83E+21 | 2.81E+21 | 2.84E+21 | 2.83E+21 | 3.13E+21 | 1.11 |
| KGT 1981 | Right center at centerline | -0.25 | 2.81E+21 | 2.77E+21 | 2.79E+21 | 2.81E+21 | 2.79E+21 | 3.18E+21 | 1.14 |
| KGT 1975 | Right edge at center line | -0.25 | 3.20E+21 | 3.15E+21 | 3.17E+21 | 3.19E+21 | 3.18E+21 | 3.44E+21 | 1.08 |
| KGT 1978 | Left edge at bottom of foil | -17.25 | 2.35E+21 | 2.34E+21 | 2.33E+21 | 2.36E+21 | 2.35E+21 | 2.27E+21 | 0.97 |
| KGT 1965 | Left center at bottom of foil | -17.25 | 2.08E+21 | 2.05E+21 | 2.04E+21 | 2.07E+21 | 2.06E+21 | 2.00E+21 | 0.97 |
| KGT 1968 | Right center at bottom of foil | -17.25 | 2.04E+21 | 2.01E+21 | 2.02E+21 | 2.04E+21 | 2.03E+21 | 2.07E+21 | 1.02 |
| KGT 1972 | Right edge at bottom of foil | -17.25 | 2.37E+21 | 2.33E+21 | 2.32E+21 | 2.35E+21 | 2.34E+21 | 2.32E+21 | 0.99 |
| KGT 1971 | Cross section at bottom of foil | -17.73 | 2.16E+21 | 2.07E+21 | 2.04E+21 | 2.08E+21 | 2.09E+21 | 2.03E+21 | 0.97 |

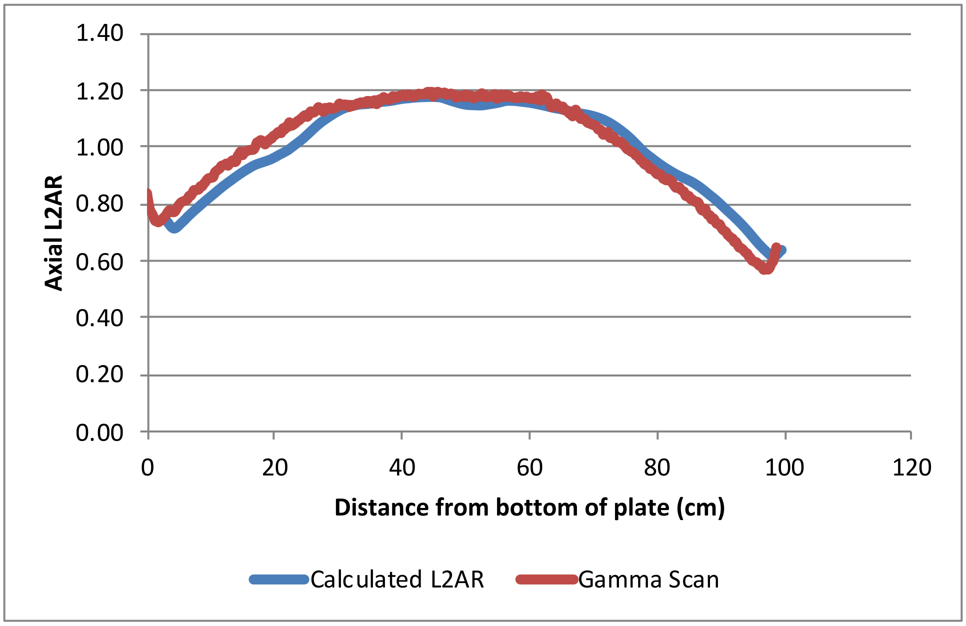

Figure 18. Calculated and measured axial profile of Plate 1.

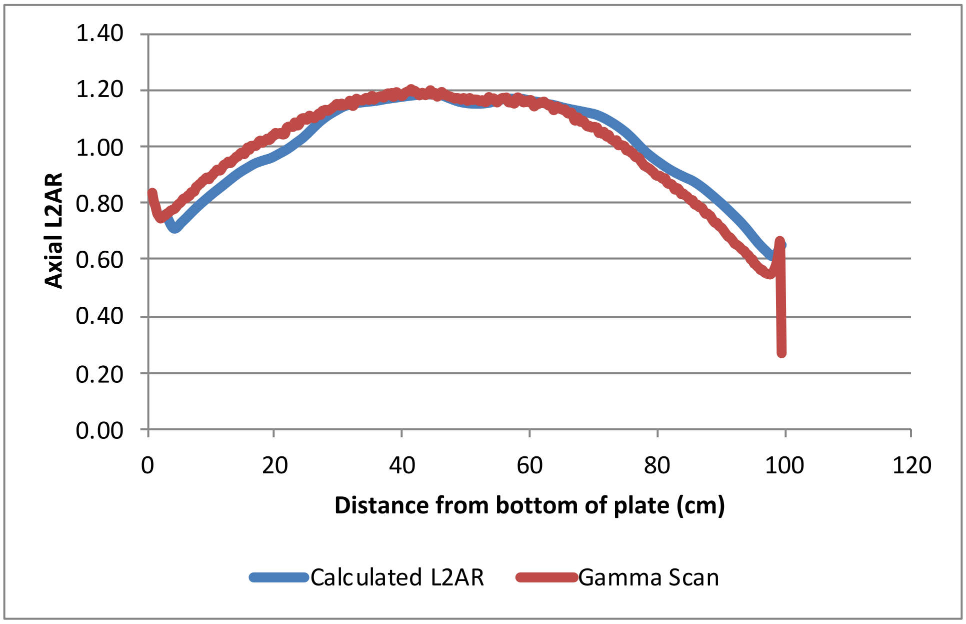

Figure 19. Calculated and measured axial profile of Plate 2.

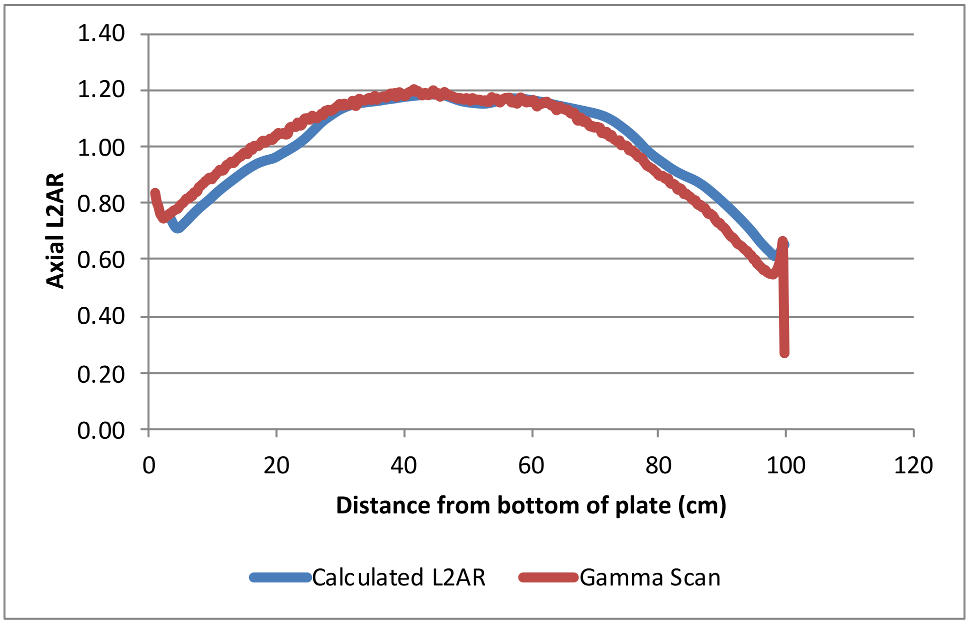

Figure 20. Calculated and measured axial profile of Plate 3.

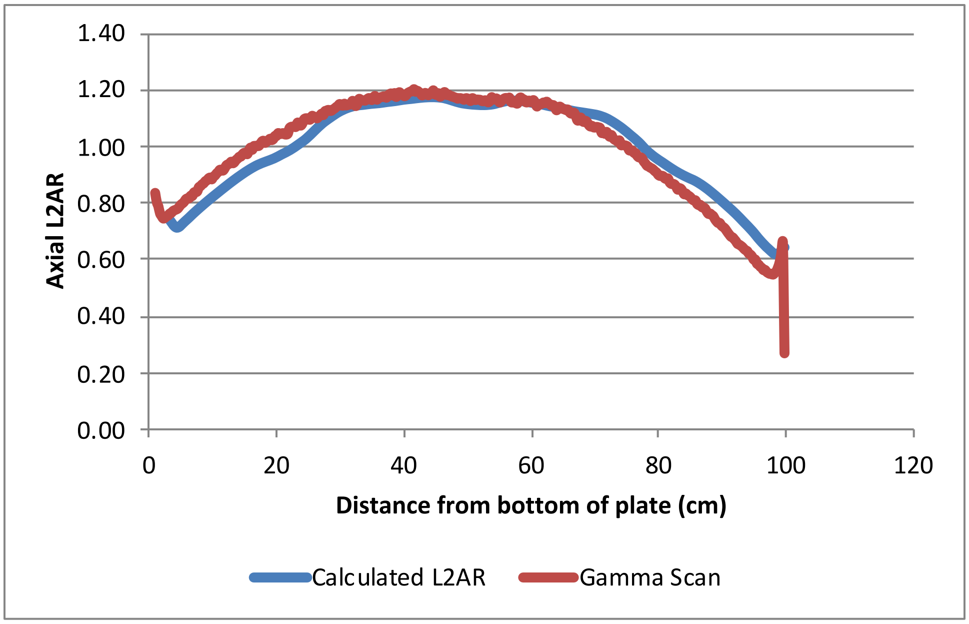

Figure 21. Calculated and measured axial profile of Plate 4.

# 7. CONCLUSIONS

The results presented above document the benchmark depletion analysis for the AFIP-7 benchmark report. The results are reported for the explicit model (e.g., best representative model) and benchmark model documented in this report. The two different models intend to demonstrate the bias of the benchmark model relative to what is considered to be the best representative model of the ATR. A comparison of the accumulated lobe exposure for the CFT is −8.7% for the benchmark model and −6.9% for the explicit model when compared to the ATR power measurements. The small difference (1.8%) between the models will not greatly affect the burnup calculations. With respect to the bias between calculated and measured values for both models, it is postulated a bias in the center lobe power may exist that has not been quantified. The lobe power monitoring system for ATR has not been updated in some time, in particular for highly fueled experiments in flux traps, which may result in additional discrepancies between the measured and calculated values.

When comparing the burnup of Plates 2 and 4, an axial bias appears to exist between the top and bottom of the plates. The fission density at the center of Plate 2 is in good agreement with the measured values. The calculated fission density for Plate 4 is approximately 10% higher than the measured values. In both plates, there is a trend of higher C/M values near the top of the plate relative to the center of the plate and lower near the bottom of the plate. This phenomenon is apparent in the gamma scan data that shows a calculated local-to-average ratio higher at the top of the plate and lower at the bottom, relative to the measured data. This may be the result of the uncertainty in knowing where the actual top and bottom edge of the fuel core is during PIE measurements. The gradient in the fission density is less near the center of the fuel plates. This would explain differences in the measured and calculated values at the top and bottom of the plates. However, a bias exists in the C/M values between Plate 2 and Plate 4, where Plate 4 is consistently higher than Plate 2 over the length of the plate. Further exploration in neutron spectrum and fission yields may provide insight into the differences between Plates 2 and 4.

The benchmark model described in this report can be used to validate other reactor physics codes. The models documented in this report demonstrate the best available model for ATR for Cycles 149B and 150B and compare those depletion results for AFIP-7 to a simplified benchmark configuration. Concerning the depletion of the AFIP-7 experiment, both models produce consistent results demonstrating that capturing the incident neutron flux of the experiment is the critical parameter for the AFIP-7 depletion benchmark.

# 8. Bibliography

[1] T. Sutton, T. J. Donovan and T. H. Trumbull, "The MC21 Monte Carlo Transport Code," in *Joint International Topical Meeting on Mathematics & Computation and Supercomputing in Nuclear Applications*, Monterey, California, 2007.

[2] S. S. Kim, "Advanced Test Reactor: Serpentine Arrangement of Highly Enriched Water-Moderated Uranium-Aluminide Fuel Plates Reflected By Beryllium," International Handbook of Evaluated Criticality Safety Benchmark Experiments.

[3] Knolls Atomic Power Laboratory, *Nuclides and Isotopes Chart of the Nuclides,* 17th Addition, 2009.

[4] A. W. H. M. R. LaPorta, "Results of Reactor Safety Analysis for Advanced Test Reactor Cycle 150B," ECAR-1660, August 2011.

[5] P. A. C. B. J. Roth, "Results of Reactor Safety Analysis for Advanced Test Reactor Cycle 149B," ECAR-1524, May 2001.

[6] J. W. Nielsen, "As-Run Neutronics Analysis for the AFIP-7 Experiment Irradiated in the Center Flux Trap of the ATR, Cycles 149B and 150B.," ECAR-1890, June 2012.

*Page intentionally left blank*

# Appendix A
# Experiment Position Loading

### A.1 ATR Experiment Positions

The ATR flux trap models documented in [2] are used in this model. Several experiments modeled in [2] have been replaced with a configuration that was more representative of the Cycle 149B and 150B models.

### A.2 North, West, Southwest, and Southeast Flux Traps

The model from Reference [2] contained a water-filled flux trap. The model contained in this report assumed a standard backup experiment in the In-Pile Tube ( IPT) experiments. This included the north, west, southwest, and southeast flux traps. The standard backup experiment consisted of a SS348 rod with a diameter of 1.5152 in. (3.848608 cm). The dimensions of the flow tube, in-pile tube, and remainder of the components were the same as [2].

### A.3 Northwest Flux Trap

The NW100 experiment is a backup experiment for the NW large in-pile tube. The experiment test train is designed to fit inside of the 4 in. (10.16 cm) hole in the in-pile tube. The backup consists of three concentric SS304 cylinders with an outer/inner radius of 1.75/1.15 in. (8.89/2.921 cm), 0.95/0.55 in. (2.413/1.397 cm), and 0.4375 in.(1.11125 cm), respectively. The inner cylinder is a solid stainless steel cylinder.

### A.4 South Flux Trap

The Advanced Graphite Capsule 2 (AGC-2) Experiment was modeled in the SFT. The experiment consists of graphite samples cooled by an inert gas inside of a graphite holder. The holders are surrounded by gas inside of a stainless steel pressure tube. The entire assembly is modeled inside of the chopped dummy in-pile tube (CDIPT). The CDIPT has an outer and inner diameter of 2.875 in. (7.3025 cm) and 2.625 in. (6.6675 cm), respectively. The pressure boundary is constructed of stainless steel with an outer/inner diameter of 2.505/2.13 in. (6.3627/5.4102 cm). Inside of the pressure tube is a 0.020 in. (0.0508 cm) thick stainless steel heat shield. The graphite holder has a diameter of 2.0672 in. (5.250688 cm). The seven graphite specimens are arranged as shown in Figure A-1 with a radial spacing from the center of 0.82 in. (2.0828 cm.) located in 0.5065 in. (1.28651 cm) holes. The graphite specimens have a diameter of 0.2505 in. (0.63627 cm). The test train is located in the safety rod guide tubes described in [2]. For modeling simplification, all materials are assumed to be uniformly modeled over the axial length of the core. This assumption will have negligible effects on the reactor model used in this benchmark report.

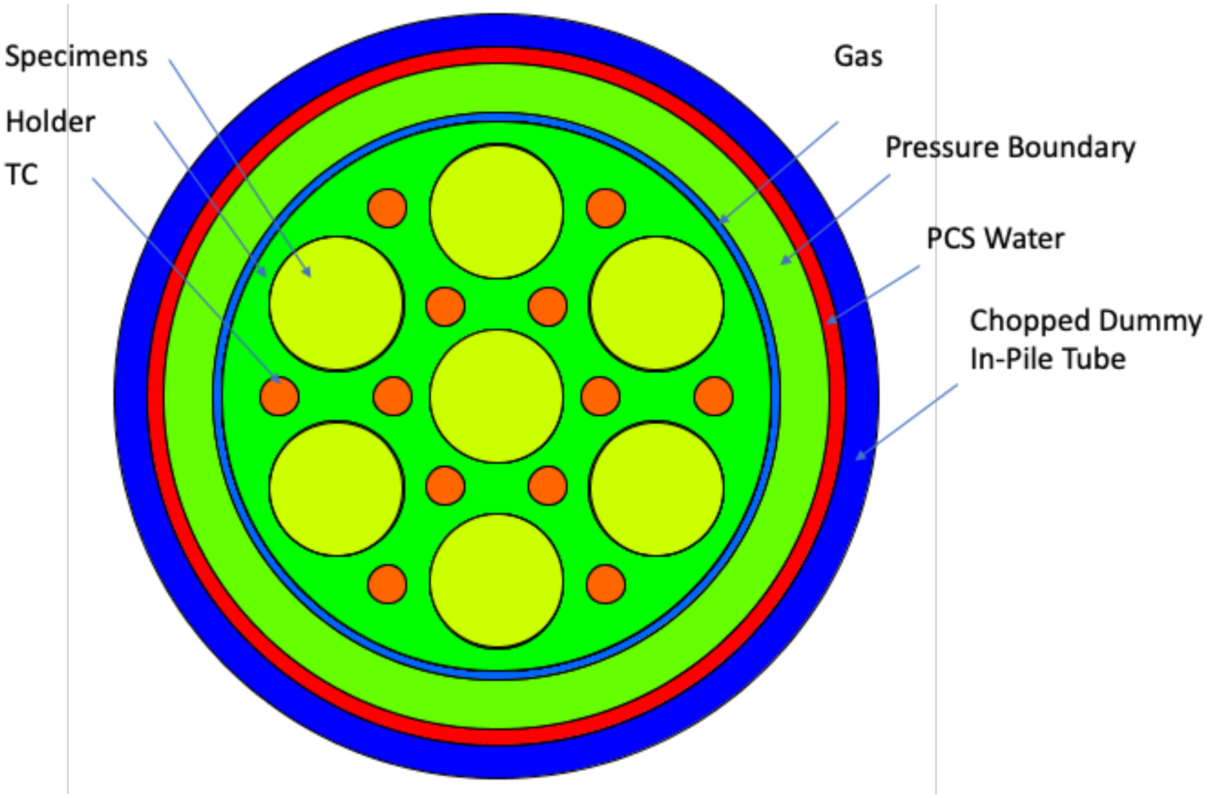

Figure A-1. Cross section of the AGC-2 experiment in the south flux trap.

### A.5 East Flux Trap

The standard irradiation housing assembly (SIHA) that was included in [2] was included in this benchmark model. The loading in Cycles 149B and 150B were different when compared to the 1994 CIC configuration. In 1994, the loading included six low specific activity cobalt capsules surrounding a flux wire monitor holder. In Cycles 149B and 150B, the model consisted of advanced fuel cycle experiments in positions 1–4 and aluminum fillers in 5–7. A diagram from [2] is shown in Figure A-2. The aluminum fillers in positions 5–7 are modeled in the SIHA guide tube, which has an outer/inner radius of 0.374/0.347 in. (0.94996/0.88318 cm). The fillers are placed in an aluminum basket with an outer/inner radius of 0.2825/0.2475 in. (0.71755/0.62865 cm). The solid aluminum filler has a radius of 0.2275 in. (0.57785 cm). The Advanced Fuel Cycle (AFC) experiments are simplified since the experiment is modeled with its cadmium basket and an aluminum filler inside. Given the presence of the cadmium filter, feedback from the small AFC rodlets will be negligible and the modeling simplification for this benchmark is adequate. The AFC baskets are constructed with a 0.305 in. (0.7747 cm) outer radius aluminum sleeve. The aluminum basket has an inner radius of 0.2150 in. (0.5461 cm). The cadmium is sandwiched in the aluminum basket with an outer/inner radius of 0.286/0.241 in. (0.72644/0.61214 cm)

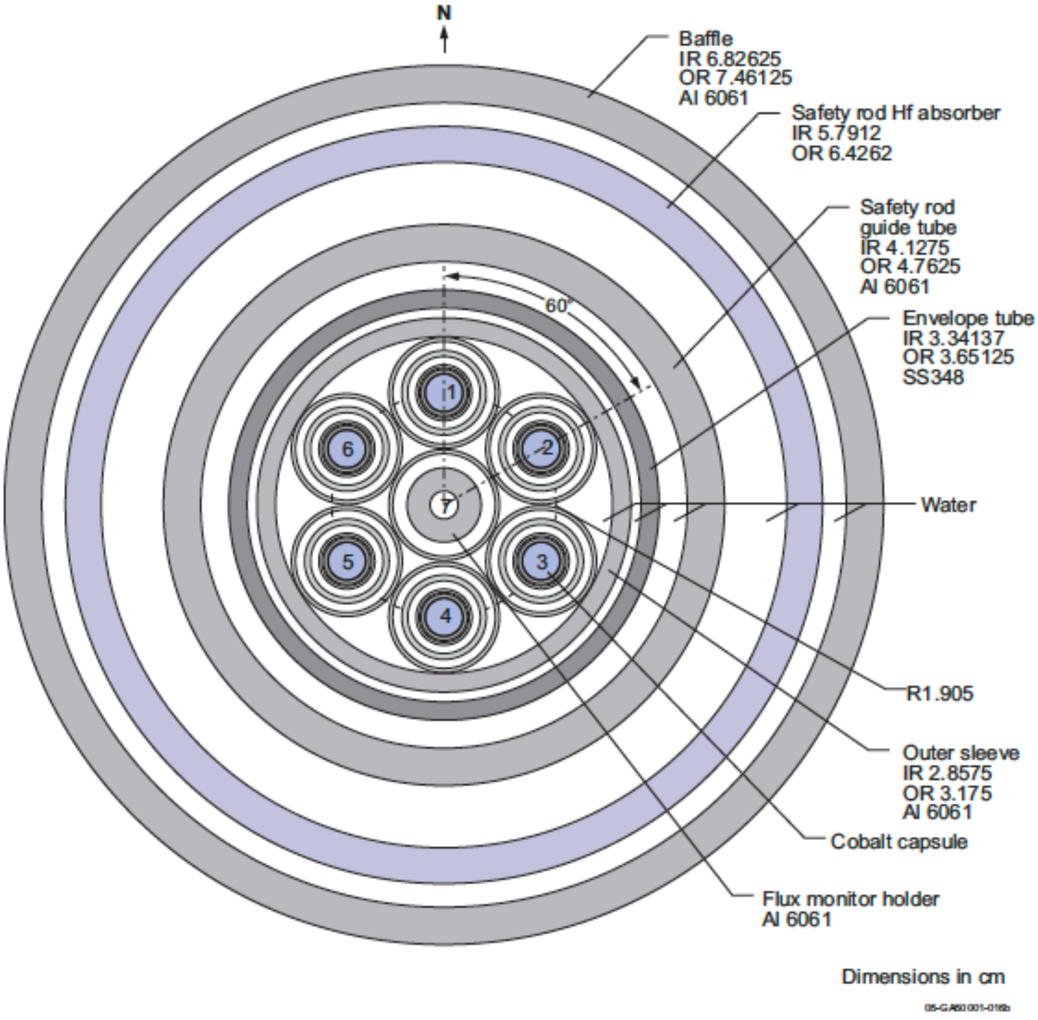

Figure A-2. Cross section of the East Flux Trap (Reference [2]) .

### A.6 High Specific Activity Cobalt

The high specific activity cobalt (HSA Cobalt) consists of a hollow aluminum tube with an inner radius of 0.125 in. (0.3175 cm). The outer radius of the tube was assumed to be 0.20491 in. (0.5204714 cm). The tube contains 4158 dimples for cobalt pellets. The tube was adjusted to allow another concentric ring with an outer radius of 0.215 in. (0.5461 cm). The radius of the tube was adjusted to preserve the mass of cobalt (29.31 grams) per target. Each target is 16.0 in. (40.64 cm) long. The active cobalt target region was assumed to be 15.0 in. (38.1 cm). The mass of cobalt in each target is assumed to be 29.13 g. Outside of the cobalt, is another aluminum tube with an outer radius of 0.240 in. (0.6096 cm), which is designed to hold the cobalt pellets into place. This configuration makes up a cobalt target. Three cobalt targets are stacked inside of an aluminum basket for use in the ATR H-positions. The aluminum basket has an outer/inner radius of 0.2825/0.240 in. (0.71755/0.6096 cm). The basket is placed inside of the ATR H-positions that have an outer radius of 0.313 in. (0.79502 cm). A cross section of the cobalt capsule in the H-baskets is presented in Figure A-3.

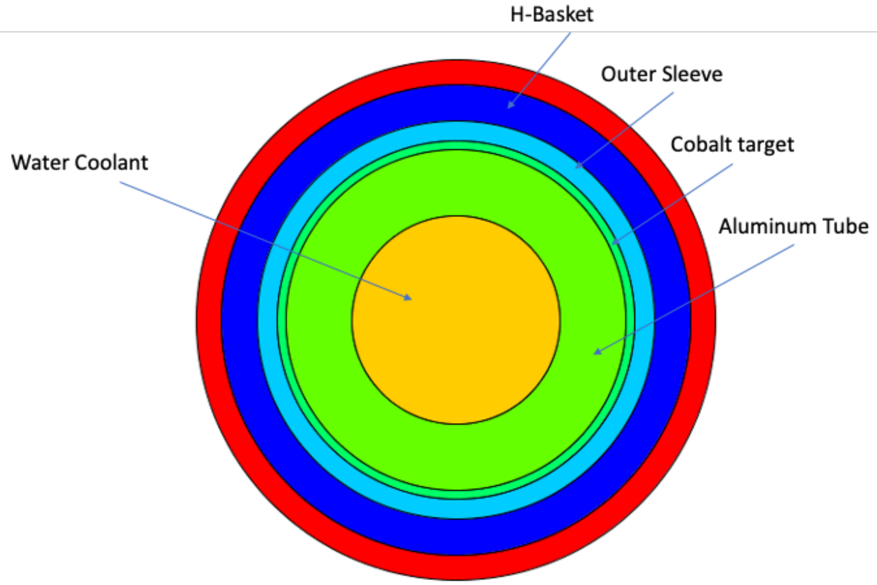

Figure A-3. H-position cobalt target cross section.

These same cobalt capsules inside of an H-basket are also used in the B-positions in ATR. In this configuration, the H-basket with three cobalt targets is placed in another aluminum basket with an outer/inner radius of 0.42/0.38 in. (1.0668/0.9652 cm). This basket assembly is placed in the small B-positions that have an outer radius of 0.4375 (1.11125 cm).

### A.7 Hafnium Shims

Four hafnium fixed shims are located in the H-positions during each operating cycle. The hafnium shims are modeled similarly to the neckshims in ATR. The hafnium shims are placed in an H-position basket with an OR/IR of 0.2825/0.2425 in. (0.71755/0.61595 cm). The hafnium shims are a solid rod with a radius of 0.173 in. (0.43942 cm). The hafnium shims are assumed to have an active absorber length of 48.0 in. (121.92 cm) with aluminum above and below the absorber that is centered about the active core in ATR.

### A.8 HSIS

The Hydraulic Shuttle Irradiation System (HSIS) is a “rabbit” facility that was located in the B-7 position. The HSIS is modeled as a 348 stainless steel tube with an outer/inner radius of 0.40/0.358 in. (1.016/0.90932 cm). The water inside and outside of the tube consists of coolant from the primary coolant system.

### A.9 AGR-2 Test

The Advanced Graphite Reactor test was designed to test graphite fuel. The test train was modeled in the B-12 positions. The model consists of a series of six capsules that are 6 in. (15.24 cm) long. Table A-1 summarizes the radial dimensions of the components as well as the materials and axial heights of each material. A cross section of the AGR-2 capsule is shown in Figure A-4 The axial heights are assigned to the cells from the bottom to the top. In other words, for materials with various axial materials, the outer and inner radius is identical; however, the axial planes bounding the cells vary with different materials.

Table A-1. AGR-2 dimensions and materials.

| Component | Material | Axial Height (Assigned from Bottom to Top) | Outer Radius | Inner Radius |
|---|---|---|---|---|
| Capsule | SS316 | 6 in. (15.26 cm) | 0.7025 in. (1.78435 cm) | 0.63825 in. (1.621155 cm) |
| Stainless steel shroud (120 degree arc) | Gas | 0.72 in. (1.8288 cm) | 0.63825 in. (1.621155 cm) | 0.638 in. (1.62052 cm) |
|  | SS316 | 5.28 in. (13.4112 cm) |  |  |
| Hafnium shroud (240 degree arc) | Gas | 0.72 in. (1.8288 cm) | 0.63825 in. (1.621155 cm) | 0.638 in. (1.62052 cm) |
|  | SS316 | 0.56 in. (1.4224 cm) |  |  |
|  | Hafnium | 4.0 in (10.16 cm) |  |  |
|  | Gas | 0.72 in. (1.8288 cm) |  |  |
| Sleeve | SS316 | 6.00 in (15.24 cm) | 0.638 in. (1.62052 cm) | 0.624 in. (1.58496 cm) |
| Gas gap | Gas | 6.00 in (15.24 cm) | 0.624 in. (1.58496 cm) | 0.6074 in. (1.542796 cm) |
| Holder | Gas | 0.72 in. (1.8288 cm) | 0.6074 in. (1.542796 cm) | ----- |
|  | SS316 | 0.285 in (0.7239 cm) |  |  |
|  | Graphite | 0.065 in. (0.1651 cm) |  |  |
|  | Gas | 0.125 in. (0.3175 cm) |  |  |
|  | SS316 | 0.085 in. (0.2159 cm) |  |  |
|  | Graphite | 4.0 in. (10.16 cm) |  |  |

Table A-1. AGR-2 dimensions and materials.

| Component | Material | Axial Height (Assigned from Bottom to Top) | Outer Radius | Inner Radius |
|---|---|---|---|---|
| | SS316 | 0.085 in. (0.2150 cm) | | |
| | Gas | 0.125 in. (0.3175 cm) | | |
| | Graphite | 0.063 in. (0.16002 cm) | | |
| | Gas | 0.067 in. (0.17018) | | |
| | SS316 | 0.38 in. (0.9652 cm) | | |
| Specimen (3 specimens 60 degrees apart on 0.3195 in. [0.81153 cm]) Radial Center | Gas | 0.72 in. (1.8288 cm) | 0.2429 in. (0.616966 cm) | ------ |
| | SS316 | 0.285 in (0.7239 cm) | | |
| | Graphite | 0.065 in. (0.1651 cm) | | |
| | Gas | 0.125 in. (0.3175 cm) | | |
| | SS316 | 0.085 in. (0.2159 cm) | | |
| | AGR Specimen | 4.0 in. (10.16 cm) | | |
| | SS316 | 0.085 in. (0.2150 cm) | | |
| | Gas | 0.125 in. (0.3175 cm) | | |
| | Graphite | 0.063 in. (0.16002 cm) | | |
| | Gas | 0.067 in. (0.17018) | | |
| | SS316 | 0.38 in. (0.9652 cm) | | |

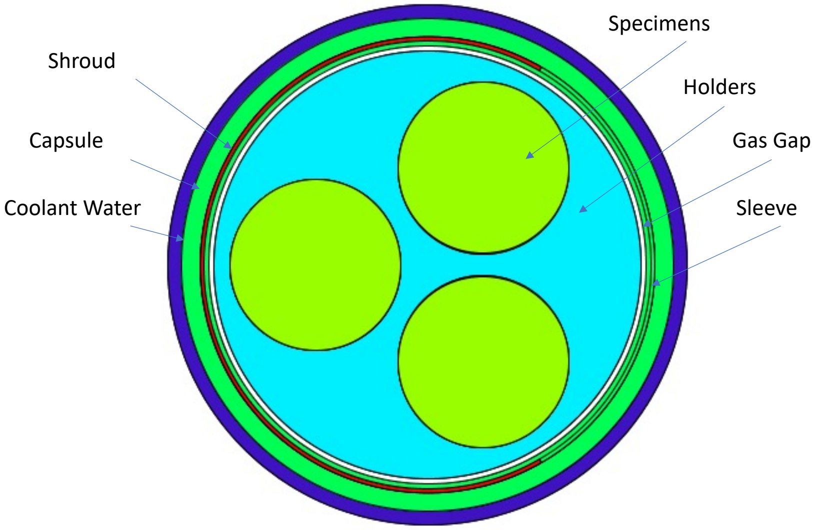

Figure A-4. Cross section of the AGR-2 Capsule.

### A.10 RERTR-12

The RERTR-12 experiment was located in B-12 position. The test train is designed to irradiate LEU mini-plates. The test train consists of four capsules stacked axially in a basket. In each capsule, there are two rows of four plates. A cross section of the RERTR-12 capsule is shown in Figure A-5. The aluminum basket is modeled with an outer/inner radius of 0.72/0.6565 in. (1.8288/1.66751 cm). Inside the basket are two guide bars to hold the capsule in place. Each guide bar is modeled as a 0.25 x 0.50 in. (0.635 x 1.27 cm) rectangle. The four capsule bodies are modeled with an axial height of 8.385 in. (21.2979 cm). The outer dimensions of the capsule body are modeled as a cylinder with a radius of 0.646 in. (1.64084 cm). The sides of the capsule body are bound by two planes at +/−0.46 in. (1.1684 cm) in the Y-plane. Inside of the capsule, a 0.62 x 0.888 in. (1.5748 x 2.25552 cm) rectangular channel. Inside of the channel are four mini-plates with a thickness of 0.055 in. (0.1397 cm) and width of 0.888 in. (2.25552 cm). The fuel core in the plates is modeled with a thickness depending upon the target conditions. The width of the fuel core is 0.75 in. (1.905 cm). The fuel loading for each of the four capsules is presented in Table A-2. Each fuel plate is 4 in. (10.16 cm) long with a 3.25 in. (8.255 cm) active fuel region.

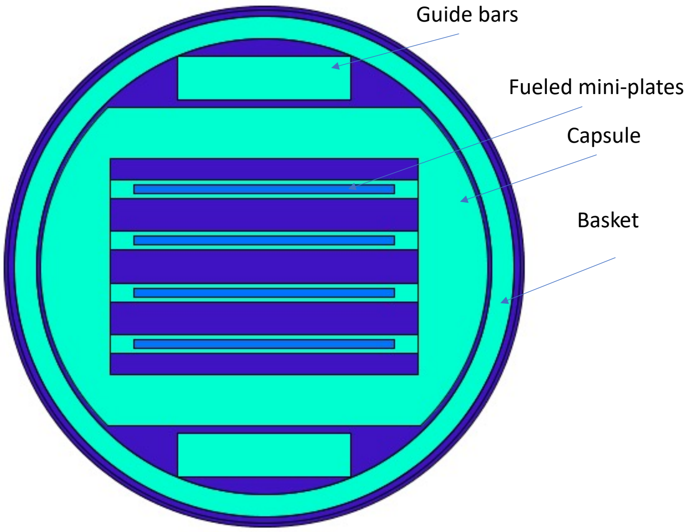

Figure A-5. Cross section of the RERTR capsule with mini-plates.

Table A-2. RERTR-12 Capsule loading for Cycle 150B.

| Capsule | Position | Thickness (mil) | U-10Mo Enrichment |
|---|---|---|---|
| D | 1 | 25 | 30 |
| | 2 | 25 | 30 |
| | 3 | 25 | 20 |
| | 4 | 25 | 10 |
| | 5 | 25 | 30 |
| | 6 | 25 | 30 |
| | 7 | 25 | 20 |
| | 8 | 25 | 10 |
| C | 1 | 25 | 30 |
| | 2 | 25 | 30 |
| | 3 | 25 | 20 |
| | 4 | 25 | 10 |
| | 5 | 25 | 30 |
| | 6 | 25 | 30 |
| | 7 | 25 | 20 |
| | 8 | 25 | 10 |
| B | 1 | Dummy Plates | |
| | 2 | | |
| | 3 | | |
| | 4 | | |
| | 5 | | |
| | 6 | | |
| | 7 | | |
| | 8 | | |
| A | 1 | 10 | 70 |
| | 2 | 20 | 40 |
| | 3 | 20 | 40 |
| | 4 | 10 | 70 |
| | 5 | 10 | 70 |
| | 6 | 20 | 40 |
| | 7 | 20 | 40 |
| | 8 | 10 | 70 |

### A.11 AFC-3

The AFC-3 experiment was modeled with the same dimensions of the AFC-2 baskets described in Section A.5. As discussed above, the aluminum filler in the basket will have negligible effects on the overall core physics. Therefore, the model of cadmium basket is sufficient.

### A.12 Small I Aluminum Filler

The small I aluminum fillers were modeled in the large B and mall I positions in the Cycle 150B model. The fillers consist of a solid aluminum rod with a radius of 0.72 in. (1.8288 cm).

# Appendix B
# Temperature Dependent Cross-Sections

As discussed above, the analysis was performed with cross-sections at 273 K. An additional set of runs was performed with the AFIP fuel cross-sections at 373 K. This provides a maximum temperature for the AFIP-7 fuel. The material for the AFIP-7 fuel plates was set at the elevated temperature. The purpose of this analysis is to determine how much of an effect Doppler broadening has on the overall result. Thermal feedback and spatially dependent temperatures have not been implemented in the ATR model at this time. This analysis can provide some indication of the effects on the results. A comparison between the Doppler broadened results and the benchmark model is presented in Table B-1 and Table B-2, for plates 2 and 4, respectively. The Doppler broadened case produced values 1 to 3% higher than the benchmark model, which is relatively small, but consistently higher. Therefore, incorporation of the thermal feedback model into the benchmark, will yield results that range from negligible to 3% higher depending upon the thermal conditions in the reactor.

Table B-1. Comparison of fission density values for Doppler Broadened cross-sections for Plate 2 (fissions/$cm^3$).

| Sample | Calculated Benchmark | Doppler Broadened | Benchmark/Doppler Broadened |
|---|---|---|---|
| KGT 1664 | 1.69E+21 | 1.71E+21 | 1.01 |
| KGT 2274 | 2.03E+21 | 2.05E+21 | 1.01 |
| KGT 2275 | 3.08E+21 | 3.13E+21 | 1.02 |
| KGT 2276 | 3.38E+21 | 3.44E+21 | 1.02 |
| KGT 2277 | 3.04E+21 | 3.09E+21 | 1.02 |
| KGT 2278 | 3.05E+21 | 3.09E+21 | 1.01 |
| KGT 2279 | 3.39E+21 | 3.43E+21 | 1.01 |
| KGT 2280 | 2.28E+21 | 2.34E+21 | 1.03 |
| KGT 2281 | 1.91E+21 | 1.96E+21 | 1.03 |
| KGT 2282 | 1.99E+21 | 2.01E+21 | 1.01 |
| KGT 2284 | 2.28E+21 | 2.33E+21 | 1.02 |
| KGT 2285 | 1.96E+21 | 2.00E+21 | 1.02 |

Table B-2. Comparison of fission density values for Doppler Broadened cross-sections for Plate 4 (fissions/$cm^3$).

| Sample | Calculated Benchmark | Doppler Broadened | Benchmark/Doppler Broadened |
|---|---|---|---|
| KGT 2488 | 1.76E+21 | 1.7763E+21 | 1.01 |
| KGT 2513 | 2.11E+21 | 2.1218E+21 | 1.01 |
| KGT 2526 | 3.18E+21 | 3.2198E+21 | 1.01 |
| KGT 2538 | 3.37E+21 | 3.4266E+21 | 1.02 |
| KGT 2550 | 3.13E+21 | 3.1789E+21 | 1.02 |
| KGT 1981 | 3.18E+21 | 3.216E+21 | 1.01 |
| KGT 1975 | 3.44E+21 | 3.4692E+21 | 1.01 |
| KGT 1978 | 2.27E+21 | 2.3265E+21 | 1.02 |
| KGT 1965 | 2.00E+21 | 2.0492E+21 | 1.02 |
| KGT 1968 | 2.07E+21 | 2.1121E+21 | 1.02 |
| KGT 1972 | 2.32E+21 | 2.3469E+21 | 1.01 |
| KGT 1971 | 2.03E+21 | 2.0709E+21 | 1.02 |

# Appendix C
# Compositions of Hafnium Control Components and Reflector

This appendix provides compositions for the hafnium control components and the beryllium reflector and beryllium in OSCC drums. The compositions for materials are contained in an attached spreadsheet. The hafnium control components are listed for under worksheets titled “149B Hafnium,” and “150B Hafnium” for cycles 149B and 150B respectively The labeling for neckshims are NS<X><Quard> where X is the neckshim number with 1 being closest to center of core and 6 furthest from the center of the core. The quadrant refers to the quadrant such as NE for northeast. OSCCs are labeled based on their quadrant (i.e., N, E, S, W) etc. and the OSCC number corresponding to the shims in that region. For each quadrant, the numbering is incrementally increased clockwise around the reactor. In other words W3, W4, N1, N2 surround the NW lobe. OSCCs N3, N4 E1, E2 surround the NE lobe etc.

The reflector is split into octants. Within each octant there are three radial regions identified as RBE, IBE, and OBE. The compositions are provided in the attached spreadsheets in worksheets titled “149B Reflector” and “150B Reflector” for cycles 149B and 150B, respectively. A cross-section of the reflector is provided in Figure C-1. The RBE region corresponds to a region close to the fuel with an outer radius of 6.564 in. from the center of the lobe and an inner radius of the flux trap. The IBE region has a inner radius of 6.564 in. and outer radius of 10.375 in. The OBE region has an inner radius of 10.375 in. from the center of the flux trap and an outer radius bounded by the reflector support tank, which is 25.75 in. from the center of the core.

The attached spreadsheet is titled “AFIP7_Control_Reflector_Compositions.xlsx.”

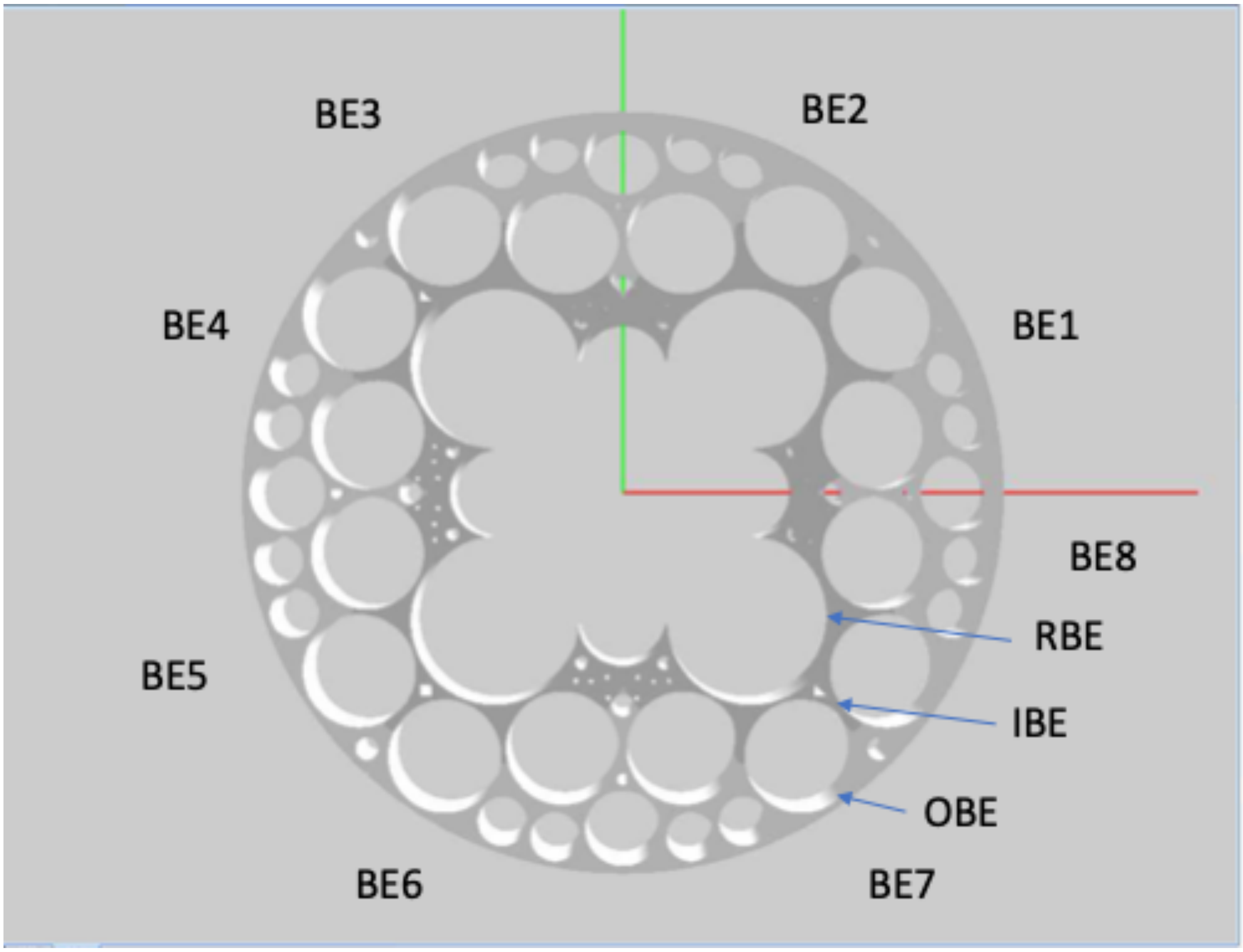

Figure C-1. Cross-section of the beryllium reflector.